Journal of the Mechanics and Physics of Solids 59 (2011) 43–63

Contents lists available at ScienceDirect

Journal of the Mechanics and Physics of Solids

journal homepage: www.elsevier.com/locate/jmps

# A closed-form, hierarchical, multi-interphase model for composites—Derivation, verification and application to nanocomposites

Yaning Li, Anthony M. Waas, Ellen M. Arruda *

*University of Michigan, Ann Arbor, MI 48105, USA*

ARTICLE INFO

*Article history:*
Received 28 April 2010
Received in revised form
10 September 2010
Accepted 26 September 2010

*Keywords:*
Interphase
Nanocomposites
Finite Element
Mori-Tanaka
Size-effects

ABSTRACT

A closed form Hierarchical Multi-interphase Model (HMM) based on the classical elasticity theory is proposed to study the influence of the interphase around inclusions on the enhancement mechanism of composites in the elastic regime. The HMM is verified by three-dimensional Finite Element simulations and highly consistent results are obtained for the cases with relatively low stiffness ratios (SR) between the inclusions and the matrix (SR $<$ 100). For cases with large SRs (up to 10,000), the HMM with the assumption of ellipsoidal inclusions provides a lower bound for the stiffnesses of composites enhanced by non-ellipsoidal particles with the same aspect ratio of inclusions. The Modified Hierarchical Multi-interphase Model (MHMM) is developed by introducing morphology parameters to the HMM, to capture the high morphology sensitivity of composites at high SRs with the non-uniform stress–strain fields. In addition, one important feature of the HMM and the MHMM is the particle-size dependency. As an application of this model to predict size effects and shape effects, the enhancement efficiencies of three typical inclusions – sphere, fiber-like particle and platelet – at different scales, are studied and compared, producing useful information about the morphology optimization at the nano-scale.



## 1. Introduction

In the framework of classical elasticity theory, Eshelby (1957, 1959 and 1961) first derived a solution for the stress and strain fields within an ellipsoidal inclusion in an infinite matrix subjected to uniform remote tractions. This solution has stood as a benchmark for extensions into several classes of problems related to finding the elastic properties of composite materials. Since the Eshelby solution neglects the interaction between inclusions, it is only suitable for composite media with very dilute concentrations of the inclusions. To overcome this drawback, the self-consistent method was originally developed, independently, by Budiansky (1965) and Hill (1965) and later extended as the generalized self-consistent method (GSCM) (Christensen and Lo, 1979; Huang et al., 1994).[1] The self-consistent method treats the matrix and inclusions equally, so it can be used for cases with very high concentrations, but the morphology of the inclusions is limited to spheres and/or short fibers; in addition, its implicit formulation makes it inconvenient to use. In parallel with these studies, the well known Mori–Tanaka method based on the original work of Mori and Tanaka (1973) was found to yield a better, explicit closed form solution for composite properties with limited information about strain or stress 'concentration factors' (Benveniste, 1987). More importantly, Tandon and Weng (1984) combined Eshelby's solution and Mori–Tanaka's average stress to obtain a closed form

* Corresponding author.
*E-mail address:* arruda@umich.edu (E.M. Arruda).

[1] See Dai et al. (1998) for a more comprehensive literature review on the self-consistent method.

0022-5096/$ - see front matter © 2010 Elsevier Ltd. All rights reserved.
doi:10.1016/j.jmps.2010.09.015

solution for finite concentrations and a large range of inclusion aspect ratios within the ellipsoidal family. Tandon and Weng (1984) presented, for example, the five independent elastic constants for a fiber reinforced tow in terms of the fiber concentration, fiber properties and matrix properties. Currently, the Mori–Tanaka (M–T) model and the semi-empirical Halpin–Tsai (H–T) model are commonly recognized as useful micromechanical models for conventional composites that have inclusions of different shapes. However, when the classical Mori–Tanaka method is used to estimate properties of nano-scale composites, it fails to accurately capture all the mechanical properties of nanocomposites (Fertig and Garnich, 2004; Sheng et al., 2004; Hbaieb et al., 2007; Liu and Brinson, 2008; Li et al., 2008a, 2008b, 2009). One possible reason is that the classical two-phase M–T model does not include the contribution of the interphase, a finite zone of material that surrounds the inclusions and is a main structural feature of nanocomposites, significantly contributing to the enhancement mechanisms of nanocomposites. Another possible reason is the dependence of effective stiffness on the morphology of non-ellipsoidal inclusions.

Depending on nanocomposite type and how it is manufactured, the existence of the interphase can be attributed to chemical, physical and/or mechanical interactions that take place during processing. Considering a polymer nanocomposite as an example, the interphase region can be formed through the interaction of matrix polymer chains and the surface molecules of inclusions either by covalent bonds (Smith et al., 2002; Yung et al., 2006) or through van der Waals forces (Jiang et al., 2006), the gyration of the polymer chain (Fossey, 2002; Baschnagel and Binder, 1995), or through the thermodynamic balance between enthalpic repulsive interactions and entropic diffusing contributions (Lipatov and Nesterov, 1997; Ginzburg and Balazs, 1999; Helfand and Tagami, 1972). In the view of continuum mechanics, the interphase is characterized by constrained polymer chains around nano-particles (Yung et al., 2006), or the presence of large strain gradients (Li et al., in press).

Many of the existing multi-phase models are for independent phases, for example, Taya and Chou (1981) and Taya and Mura (1981) extended the two-phase M–T model to three phases to study composites with two independent sets of inclusions. Other methods for the cases with limited inclusion morphology include the GSCM three-phase sphere model (Christensen and Lo, 1979; Huang et al., 1994). Ji et al. (2002), Sarvestani (2003), Shodja and Sarvestani (2001) and Wu et al. (1999) each individually proposed a three-phase model, representing particles encapsulated in another phase (coating and/or interphase) and then in a matrix. Unfortunately, most of these models are simplified analytical models without enough consideration given to the particle morphology and therefore none of them is applicable to nanocomposites reinforced by particles with large aspect ratios.

There is a controversy in modeling composites reinforced by ellipsoidal inclusions versus non-ellipsoidal ones, as evident in the past literature. Eshelby (1957) showed the remarkable property of ellipsoidal inclusions that the elastic field inside an ellipsoidal inclusion of uniform eigenstrain is constant. Eshelby (1961) conjectured that non-ellipsoidal inclusions do not have this property. Mura et al. (1994) claimed that pentagonal inclusions are similar to the ellipsoids in the sense of this property. However, Rodin (1996) and Markenscoff (1998) proved that non-ellipsoidal inclusions cannot have this property. Nozaki and Taya (1997) proposed a method to estimate the effective stiffness of a composite with polygonal inhomogeneities. Their method was flawed in that it neglected the non-constant Eshelby's tensor for non-ellipsoidal inclusions with uniform eigenstrain (see Rodin, 1998). Nozaki and Taya (2001) later showed that for polygonal and polyhedral inclusions, although this unique property of ellipsoidal inclusions does not hold in an exact sense, a good estimation can be obtained when assuming this property could be extended to nonellipsoidal inclusions, and when the number of sides in the polygon increases and/or the stiffness difference between the polygon material and the matrix becomes small, good accuracy can be obtained. Thus, these controversial arguments in the past literature show an intrinsic consistency. In this investigation, this intrinsic consistency will be confirmed numerically and the morphological sensitivity of non-ellipsoidal inclusions to the effective stiffness of the composites reinforced by them will be studied.

In addition, there is a serious drawback in the M–T model: size-independency. The size effect of nanocomposites is such that for the same volume fraction of inclusions, if the inclusion size decreases, material properties such as strength and modulus dramatically increase. However, this size effect cannot be captured by conventional methods including the M–T model mentioned above, because these methods have no length scale included. Several researchers (Vernerey et al., 2008; Liu and Brinson, 2006; Liu and Hu, 2005; Tan et al., 2005; Sharma and Ganti, 2004; Barnard and Curtiss, 2005; Lim, 2003; Lim, 2005) have examined the particle size effects in composites. For example, Lim (2003, 2005) included interatomic energy at the interface of the matrix and the inclusion in his model to study how nano-scale inclusions influence the mechanical properties of the nanocomposites. Sharma and Ganti (2004) modified Eshelby's tensor of spherical and cylindrical inclusions with surface energy incorporated via a continuum field formulation of surface elasticity.

This paper is organized as follows. In Section 2, we derive a closed form solution for composites enhanced by particles and a hierarchical, multi-layered interphase based on the Mori–Tanaka method, specifically, by using Tandon and Weng's (1984) approach. In Section 3, this hierarchical, multi-layered interphase model (HMM) is verified by three-dimensional Finite Element (FE) simulation. If the stiffness ratio (SR) between the inclusion and the matrix is less than $\sim$100, a range we describe as Range 1, 3-D FE simulations verify that this model can accurately predict the elastic properties of composites with one interphase layer and finite volume fractions. Many of the existing models, either analytical or numerical, have been verified only in this range of relatively small SR values ($<100$, for example, Tandon and Weng, 1984, 1986; Benveniste, 1987; Huang et al., 1994; Dai et al., 1998; Fertig and Garnich, 2004; Hbaieb et al., 2007). For composites with larger values of SR (100–10,000), the enhancement efficiency[2] of the fillers becomes very sensitive to the morphology of

[2] The definition of enhancement efficiency can be found in Section 3.1.

the filler. If the value of SR is large enough, strongly non-uniform stress–strain fields will be formed due to the non-ellipsoidal morphology of the inclusion. This non-uniformity violates the premise of uniform stress and strain fields in the phases, as assumed in the Mori–Tanaka method. Since the HMM has the same premise as the M–T model, it is not suitable to be used for cases with large values of SR. Therefore, a Modified Hierarchical Multi-interphase Model (MHMM) is proposed here to take the non-uniformity effect into consideration, which is illustrated in Section 4. One important feature of the HMM and the MHMM is their particle size-dependency. The prediction of size effects is addressed as an application of the HMM and the MHMM in Section 5. The prediction results show that particle size-dependency of composites depends on the interphase properties, and on the morphology and aspect ratio of the inclusion. The interphase layers make a critical contribution to the size effects based on the HMM and the MHMM, which is explained by relating the interphase to the surface-to-volume ratio of the inclusion. In addition, the particle shape effects are studied as well. The size effects of the enhancement efficiency of three typical fillers – spheres, fibers and platelets – are studied and compared, producing useful information for morphology optimization.

## 2. Derivation of the Hierarchical Multi-interphase Model (HMM)

Real composites are complicated due to the number and the arrangement of the reinforcing phases, and the shapes, orientations and spatial distributions of inclusions. Currently, composite models that can be applied to the most general case that includes all these variations do not exist. As far as the multi-phase composites are considered, two types of multi-phase composites exist with respect to the arrangements of various phases: the independent multi-phase composites in which the reinforcing phases are embedded in the same matrix independently from each other, as shown in Fig. 1a; and the hierarchical multi-phase composites in which the inclusions are coated with multi-interphases hierarchically, as shown in Fig. 1b. The differences between these two types of composites were also observed by Liu and Brinson (2006). A more general type of multi-phase composite is a combination of these two types, as shown in Fig. 2, in which the hierarchically arranged phases are embedded in the matrix independently. This type of multi-phase composite can be modeled by including the influence of independent multi-phases and that of hierarchical multi-phases.

The Mori–Tanaka model for the independent multi-phase composite has been introduced by Liu and Brinson (2006). If the independent phases are similar in shape and are of either uniform orientation or random orientation, the stiffness tensors of the aforementioned model are diagonally symmetric (Schjodt-Thomsen and Pyrz, 2001; Chen et al., 1990; Benveniste et al., 1989). But the stiffness tensors predicted by the M–T model for composites containing inclusions of various shapes,

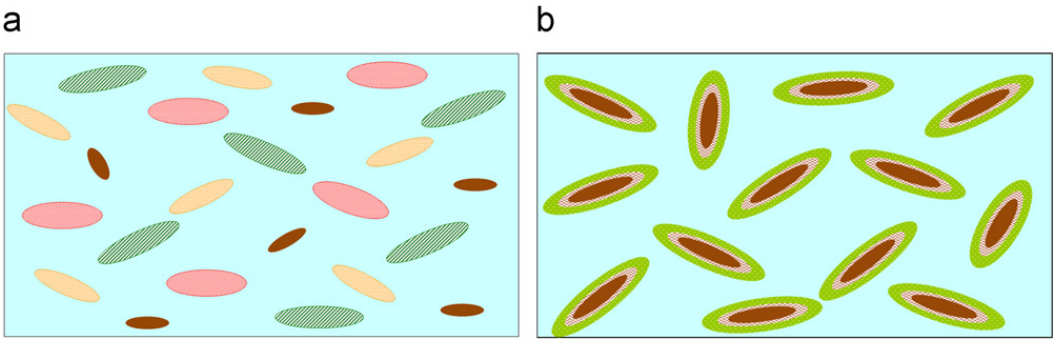


**Fig. 1.** Sketches of the two types of multi-phase composites (different colors and patterns represent different phases). (a) Independent multi-phase composites and (b) hierarchical multi-phase composites. (For interpretation of the references to color in this figure legend, the reader is referred to the web version of this article.)

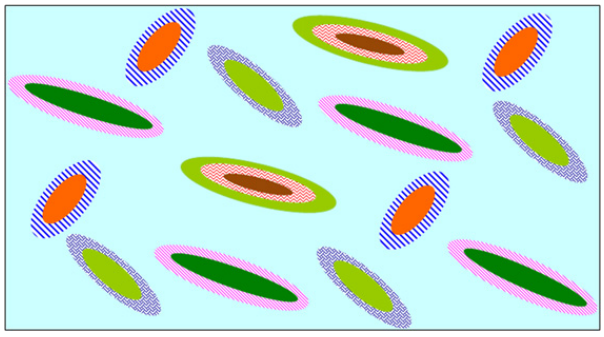

**Fig. 2.** Sketch of a more general type of multi-phase composites (different colors and patterns represent different phases).

orientations and spatial distributions can be asymmetric (Casteneda and Willis, 1995; Li, 1999; Benveniste et al., 1991a). Corrections and modifications of the M–T method and also alternative methods were proposed by several researchers because of these limitations (Casteneda and Willis, 1995; Berryman and Berge, 1996; Schjodt-Thomsen and Pyrz, 2001).

However, Benveniste et al. (1991b) found that if the 'typical inclusion' is a coated particle, then the implementation can be carried out within the framework of two-phase composites and thus gives a diagonally symmetric stiffness tensor (Benveniste et al., 1989; Chen et al., 1990; Li, 1999). Thus a hierarchical multi-phase composite model can be derived using the M–T approach without violating the symmetry requirement of the elastic stiffness tensor.

Before deriving the HMM, the existing model of Liu and Brinson (2006) for composites with $N$ types of independent phases will be briefly summarized in Section 2.1 for comparison with the HMM derived later in Section 2.2. Later, these two models will be combined to derive a more general type of multi-phase composite as shown in Fig. 2. Although this independent multi-phase M–T model (Liu and Brinson, 2006) has the aforementioned limitations, it can be served as an example to illustrate how the present hierarchical multi-phase composite model can incorporate independent multi-phase composite models to obtain models for a more general case including both hierarchical and independent multi-phases.

With this example, for an even more general type of composite, including various inclusion shapes, orientations and spatial distributions, the explicit models can be easily obtained by the readers by replacing the model of Liu and Brinson (2006) with other explicit models, for example, one including effects of various inclusion shapes and spatial distributions (Castaneda and Willis, 1995) or one including effects of various inclusion orientations (Tandon and Weng, 1986; Schjodt-Thomsen and Pyrz, 2001).

### 2.1. Independent multi-phase Mori–Tanaka model

Benveniste (1987) showed that Tandon and Weng's (1984) closed-form solution can be written in a compact form by using Hill's concept of a strain concentration tensor. Using this concept, Liu and Brinson (2006) wrote the stiffness tensor for the case with $N$ types of independent inclusions explicitly. In this section, this analysis is summarized briefly. In terms of interactions between inclusions, for one reinforcement phase, it is assumed that the inclusion can sense the strain in the matrix. Therefore we have

$$\underline{\varepsilon}^1 = \underline{T}\underline{\varepsilon}^0, \tag{1}$$

and

$$\underline{T} = \left[I + \underline{S}\left(\underline{C}^0\right)^{-1}(\underline{C}^0 - \underline{C}^1)\right]^{-1}, \tag{2}$$

where $\underline{\varepsilon}^1$ and $\underline{\varepsilon}^0$ are the uniform strain tensors in the inclusion and the matrix, respectively. $\underline{T}$ is the dilute concentration tensor, $\underline{C}^0$,$\underline{C}^1$ are the elastic stiffness tensors of the matrix and inclusion. $\underline{S}$ is the Eshelby transformation tensor, and $\underline{I}$ is the identity tensor (Benveniste, 1987).

By calculating the average stress $\overline{\sigma}$ and strain $\overline{\varepsilon}$ in the composite ($\overline{\sigma} = \underline{C}\overline{\varepsilon}$), the stiffness of the composite $\underline{C}$ is found to be

$$\underline{C} = \left(f^0\underline{C}^0 + f^1\underline{C}^1\underline{T}\right)\left(f^0\underline{I} + f^1\underline{T}\right)^{-1}, \tag{3}$$

or alternatively expressed as (Benveniste, 1987; Liu and Brinson, 2006),

$$\underline{C} = \underline{C}^0 + f^1\left[\left(\underline{C}^1 - \underline{C}^0\right)\underline{T}\right]\left(f^0\underline{I} + f^1\underline{T}\right)^{-1}, \tag{4}$$

where $f^0$ and $f^1$ are the volume fraction of the matrix and the inclusion. Eqs. (3) and (4) are equivalent, however, the form Eq. (3) is used here, since it is consistent with Eq. (5). This compact explicit expression of the stiffness tensor is equivalent to Tandon and Weng's (1984) step-by-step derivation.

For more general cases in which **N** independent inclusions are distributed in the matrix, the stiffness tensor was derived by Liu and Brinson (2006) as

$$\underline{C}_N = \left[f^0\underline{C}^0 + \sum_{j=1}^{N} f^j\underline{C}^j\underline{T}^j\right]\left[f^0\underline{I} + \sum_{j=1}^{N} f^j\underline{T}^j\right]^{-1}. \tag{5}$$

### 2.2. Hierarchical Multi-interphase Model (HMM)

Consider a composite with the matrix material reinforced by a certain type of inclusion, and with a region of interphase formed around the inclusions either chemically or physically. If the dimensions and the structure of the interphase region and the mechanical properties of it are known, what would be the average mechanical properties of the composite? Similar to Tandon and Weng's (1984) approach, constant tractions are maintained at the far-field boundaries of the bulk matrix material, and therefore a uniform strain field is generated in it. After adding the interphase, not only is the strain field in the matrix perturbed, but the strains in the interphase and the inclusion are perturbed as well. The interaction between the inclusion and the matrix is not direct but through the interphase. The interphase not only passes the stress–strain perturbation due to the

matrix to the inclusion but also brings a second perturbation to the inclusion directly due to itself. Thus, the perturbations are passed hierarchically from the very outside (matrix) to the very inside (inclusion). This process is illustrated with details in Appendix A. Thus, different from the independent multiple phase model, discussed in Section 2.1, in which all other phases interact with the matrix directly and equally, in the present multi-interphase model, all phases interact hierarchically.

In this section, a closed form solution for the Hierarchical Multi-interphase Model (HMM) is derived. The derivation begins with the case of only one homogenous interphase layer. Before initiating the derivation, the notations are defined: the notations with a symbol '_' represent tensors; the superscripts '$m$', '$i$' and '$p$' represent the matrix, the interphase and the particle/inclusion/filler, respectively. For example, $\underline{\varepsilon}^m$, $\underline{\varepsilon}^i$ and $\underline{\varepsilon}^p$ are the strain tensors in the matrix, the interphase and the particle. Since only phases contacting each other can interact directly and sense the strains of each other, the interactions are pair-wise. Between the interphase and matrix phases,

$$\underline{\varepsilon}^i = \underline{T}^{im}\underline{\varepsilon}^m, \tag{6}$$

in which $\underline{T}^{im}$ is the strain concentration tensor between the interphase and the matrix,

$$\underline{T}^{im} = \left[\underline{I} + \underline{S}^1(\underline{C}^m)^{-1}(\underline{C}^m - \underline{C}^i)\right]^{-1}, \tag{7}$$

where $\underline{C}^m$, $\underline{C}^i$ are the stiffness tensors of the matrix and the interphase, respectively; $\underline{I}$ is the identity tensor; and $\underline{S}^1$ is the Eshelby's transformation tensor of an imaginary two-phase composite, in which the material of the particle was replaced by the material of the interphase. The expression for $\underline{S}^1$ is provided by Tandon and Weng (1984) as a function of inclusion aspect ratio. Between the phases of the inclusion and the interphase,

$$\underline{\varepsilon}^p = \underline{T}^{pi}\underline{\varepsilon}^i, \tag{8}$$

in which $\underline{T}^{pi}$ is the strain concentration tensor between the inclusion and the interphase,

$$\underline{T}^{pi} = \left[\underline{I} + \underline{S}^2\left(\underline{C}^i\right)^{-1}(\underline{C}^i - \underline{C}^p)\right]^{-1}, \tag{9}$$

where $\underline{C}^p$ is the stiffness tensor of the inclusion, $\underline{S}^2$ is the Eshelby's transformation tensor (see Tandon and Weng, 1984) of an imaginary two-phase composite in which the matrix is removed, only the phases of interphase and particle are left.

Combining Eqs. (6) and (8), a relationship between the strain of the matrix and the strain of the inclusion is expressed by

$$\underline{\varepsilon}^p = \underline{T}^{pi}\underline{T}^{im}\underline{\varepsilon}^m. \tag{10}$$

Therefore, via again establishing what the volume-averaged stress and strain tensors are in the composite, this leads to

$$\overline{\underline{\sigma}} = f^m\underline{\sigma}^m + f^i\underline{\sigma}^i + f^p\underline{\sigma}^p = f^m\underline{C}^m\underline{\varepsilon}^m + f^i\underline{C}^i\underline{\varepsilon}^i + f^p\underline{C}^p\underline{\varepsilon}^p, \tag{11}$$

and

$$\overline{\underline{\varepsilon}} = f^m\underline{\varepsilon}^m + f^i\underline{\varepsilon}^i + f^p\underline{\varepsilon}^p \text{ and } f^m + f^i + f^p = 1, \tag{12}$$

where $\underline{\sigma}^m$, $\underline{\sigma}^i$ and $\underline{\sigma}^p$ are the stress tensors in the matrix, the interphase and the particle, respectively, $f^m$, $f^i$ and $f^p$ are the volume fractions, and taking the composite as a homogeneous continuum, $\overline{\underline{\sigma}}$, $\overline{\underline{\varepsilon}}$ are the average stress and strain tensors and $\underline{C}$ is the composite stiffness,

$$\overline{\underline{\sigma}} = \underline{C}\overline{\underline{\varepsilon}}. \tag{13}$$

Combining Eqs. (11)–(13), the stiffness tensor of the composite is written as

$$\underline{C} = \left[f^m\underline{C}^m + f^i\underline{C}^i\underline{T}^{im} + f^p\underline{C}^p\underline{T}^{pi}\underline{T}^{im}\right]\left[f^m\underline{I} + f^i\underline{T}^{im} + f^p\underline{T}^{pi}\underline{T}^{im}\right]^{-1}. \tag{14}$$

If $\underline{C}^m = \underline{C}^i$, i.e. $\underline{T}^{im} = \underline{I}$ , Eq. (14) degenerates into the classical two-phase M–T model with a particle volume fraction equaling $f^p$; if $\underline{C}^i = \underline{C}^p$, i.e. $\underline{T}^{pi} = \underline{I}$ , it degenerates into the M–T model with a reinforcement volume fraction equaling $f^i + f^p$. Eq. (14) is written in a compact form using the concept of strain concentration tensors. The conceptually equivalent step by step derivation (as in Tandon and Weng, 1984) is shown in Appendix A.

To account for the more realistic and general cases, a model with $K-1$ layers of homogenous interphase is derived as follows.

Assume that the 0th phase is the matrix, the $K$th phase is the inclusion, and there are $(K-1)$ layers of interphase ordered as 1th to $(K-1)$th from the outside to inside (from the phase closest to the matrix to that closest to the inclusion). The stiffness tensors and volume fractions of all the phases are represented as $\underline{C}^0, \underline{C}^1, \ldots, \underline{C}^k, f^0, f^1, \ldots, f^k$, respectively. Then, the hierarchical interaction between the $j$th phase and the $(j-1)$th phase can be expressed by[3]

$$\underline{\varepsilon}^j = \underline{T}_i^j\underline{\varepsilon}^{j-1}, \tag{15}$$

[3] The subscript '$i$' is used in $\underline{T}_i^j$ and some other notations in Eqs. (15)–(18) to make a distinction between the current notations and those describing the independent multi-phase model, used in Section 2.1.

in which

$$\underline{T}_i^j = \left[\underline{I} + \underline{S}_i^j \left(\underline{C}^{j-1}\right)^{-1} \left(\underline{C}^{j-1} - \underline{C}^j\right)\right]^{-1}, \tag{16}$$

where $\underline{S}_i^j$ is the Eshelby tensor for the imaginary two-phase composite with phases outside the $(j-1)$th phase removed and phases inside the $j$th phase replaced by the material of the $j$th phase. The expression of Eshelby tensor is provided by Tandon and Weng (1984) as a function of inclusion aspect ratio. Thus the strain of the inclusion is related to that of the matrix through $j-1$ layers of interphase as

$$\underline{\varepsilon}^j = \underline{T}_i^j \underline{T}_i^{j-1} \ldots \underline{T}_i^1 \underline{\varepsilon}^0 = \left(\prod_1^j \underline{T}_i^j\right) \underline{\varepsilon}^0. \tag{17}$$

It should be noted that the order of the multiplication of the strain concentration tensors, from $j$ to 0, represents the order from inside (the inclusion) to outside (the matrix). Thus, the total stiffness tensor of the composite can be written as

$$\underline{C}_i = \left[f^0 \underline{C}^0 + \sum_{j=1}^{K} f^j \left\{\underline{C}^j \left(\prod_{j=1}^{K} \{\underline{T}_i^j\}\right)\right\}\right] \left[f^0 \underline{I} + \sum_{j=1}^{K} f^j \left(\prod_{j=1}^{K} \{\underline{T}_i^j\}\right)\right]^{-1}, \tag{18}$$

in which '$\{\bullet\}$' represents the orientation-average of the tensor inside, following Liu and Brinson's (2006) definition. By replacing the $\underline{C}^j$ of each independent inclusion in Eq. (5) with the $\underline{C}_i^j$ defined in Eq. (18), a more general case of the composite with $N$ types of independent inclusions and each inclusion with $K$ multi-layer interphases (see Fig. 2) can be obtained.

## 3. Verification of the Hierarchical Multi-interphase Model (HMM)

### 3.1. Three dimensional Finite Element simulation

In this section, the HMM is verified by FE simulations of Representative Volume Elements (RVE) of nanocomposites reinforced by aligned nano-platelets with an aspect ratio of 100. Both two-dimensional (2D) plane strain FE model and three-dimensional (3D) FE model prevail in the current research community to model nanocomposites (Bradshaw et al., 2003; Fertig and Garnich, 2004; Sheng et al., 2004; Hbaieb et al., 2007; Liu and Brinson, 2008; Li et al., 2008a, 2008b, in press). 3D FE models are used in this study for the purpose of better accuracy. 3D FE RVEs of six nanocomposite-structure RVEs have been generated (Table 1). The shapes of the RVEs are prisms with a $124.5 \times 124.5$ nm$^2$ cross section in the 1–2 plane. The inclusion is also a prism, having a $100 \times 100$ nm$^2$ cross section and a thickness of 1 nm. Thus the aspect ratio of the inclusion is 100. These RVEs chosen have a similar structures with the polyurethane–montmorillonite clay

**Table 1**
FE model of the RVEs.

| Particle vol% ($f_p$) | Matrix; Inclusions; Interphase | |
|---|---|---|
| | No interphase | With interphase |
| 2.5 | 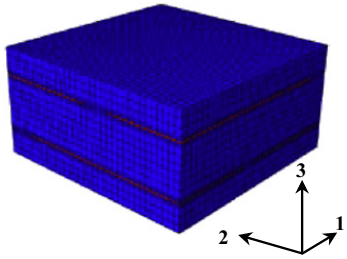  | 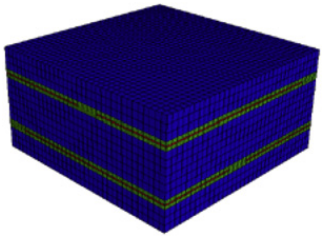 |
| 5 | 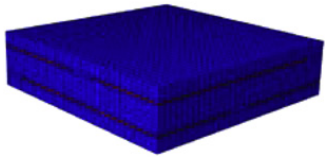 | 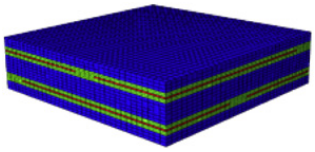 |
| 10 | 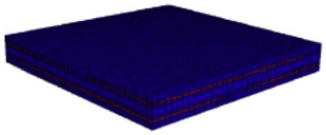 | 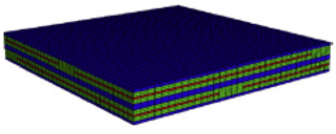 |

nanocomposites manufactured in our laboratory (Podsiadlo et al., 2007; Podsiadlo et al., 2008; Li et al., 2008a, 2008b, 2010; Kaushik et al., 2009). In order to simulate the non-uniform stacking of nanocomposites in the 3 direction, each RVE has offset particles. The details of choosing the RVE are explained by Li et al. (in press). By adjusting the distance between the two particles, RVEs with different volume fractions are obtained. Interphase layers around the inclusions with a constant thickness of 2 nm are assumed in all cases. All phases are assumed to be perfectly bonded. 3D periodic boundary conditions are applied at the boundaries of the RVEs. The details of similar boundary conditions can be found in Li et al. (in press).

In order to obtain the longitudinal stiffness of the composite, displacements in the 1 direction are controlled in the FE simulations to simulate uni-axial tension. The displacement-controlled loading condition is coupled with the periodic boundary conditions, as explained by Li et al. (in press). Uni-axial strain of a RVE (up to 1.5% in the simulations) is obtained by controlling the displacement. The corresponding uni-axial stress equals the average stress on the cross section of the boundaries. Nanostructures of this RVE type lead to an orthotropic stiffness matrix with $E11=E22$. We will focus on these equal in-plane elastic moduli. Then the in-plane elastic modulus of the composite is obtained, denoted as $Ec$. The enhancement efficiency of the composite is defined as $Ec/E0$, where $E0$ is the matrix stiffness. Nanocomposites of 2.5, 5.0 and 10.0 vol% particles ($f_p$) are chosen for the simulations; the corresponding interphase fractions ($f_i$) are 5.15, 10.3 and 20.6 vol%. The elasticity of the nanocomposites is examined with and without the interphase region.

In all simulations, the phases are isotropic and are assumed elastic. The Young's moduli of the matrix and interphase are $E0=25$ MPa and $Ei=75$ MPa, respectively, and the Poisson's ratios are assumed the same and equal to 0.48. To represent cases in a wide range of particle to matrix stiffness ratios (SRs), the Young's modulus of the particle $E1$ varies over a large range in the simulations: 125 MPa, 250 MPa, 500 MPa, 2.5 GPa, 25 GPa and 250 GPa (giving SR ($E1/E0$): 5, 10, 20, 100, 1000 and 10,000). The Poisson's ratio of the particle is 0.375. A comparison of the predicted results from the HMM and the 3D FE simulations is shown in Fig. 3, which shows that for the cases with low particle volume fractions or low SRs ($E1/E0$), the HMM can predict the enhancement efficiency of the composite accurately: for example, for a low volume fraction of 2.5%, the model is accurate over the entire SR range; for larger volume fractions, 5% and 10%, the model is accurate when SR is less than 100. Many existing analytical composite models have been verified up to SR=100 (Tandon and Weng, 1984; Benveniste, 1987; Christensen and Lo 1979; Huang et al., 1994; Dai et al., 1998), because the SRs of the traditional composites have typically fallen in this range. Fig. 3 also shows that the enhancement efficiency of composites increases nonlinearly with SRs: for low SRs (1–100), or Range 1, the increment is slow; for large SRs (100–10,000), Range 2, the increment is rapid, such that a big jump of the enhancement efficiency occurs; for even larger SRs ($>10{,}000$), the increment slows down, which implies that the enhancement efficiency approaches its asymptotic limit, and it cannot be improved any more no matter how large the SR is. Many traditional composites fall in Range 1. Some new materials, such as polymer composites with nano-particles, fall in the Range 2 and very high values of SRs are achieved. For example, the Young's modulus of nanotubes can reach 1 TPa, and that of nano-particles of clay can reach 250 GPa (Podsiadlo et al., 2007; Li et al., 2008a, 2008b, in press; Kaushik et al., 2009), while the Young's modulus of the polymer matrix may be on the order of $10–10^2$ MPa. The development of nanocomposites shows a need for composite models covering a large range of SRs. Unfortunately, little information can be found in Range 2 of SRs in the open literature; little experimental data can be found, and much of the Finite Element analysis of nanocomposites does not cover this range either (Fertig and Garnich, 2004; Sheng et al., 2004; Hbaieb et al., 2007; Liu and Brinson, 2008). The current study contributes to this important Range 2. The difficulties in studying composites in Range 2 lie in the fact that the enhancement mechanisms become more

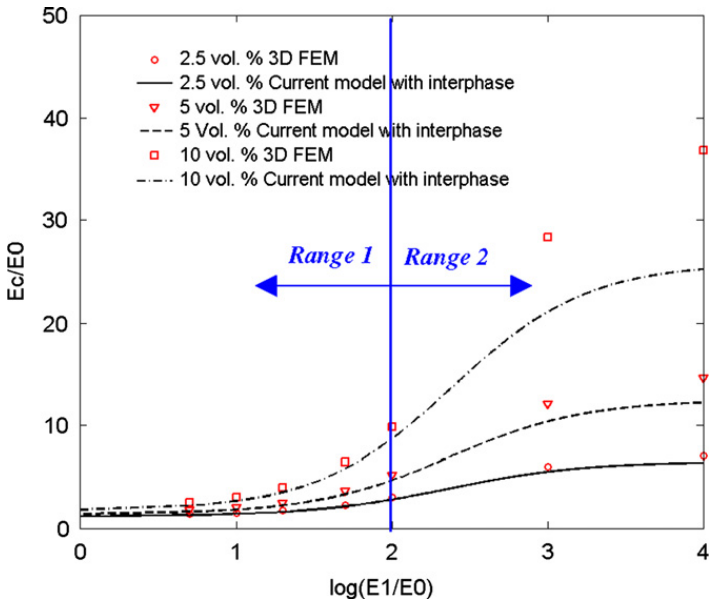


**Fig. 3.** Comparison of the predicted results of the HMM and the 3D FE simulations.

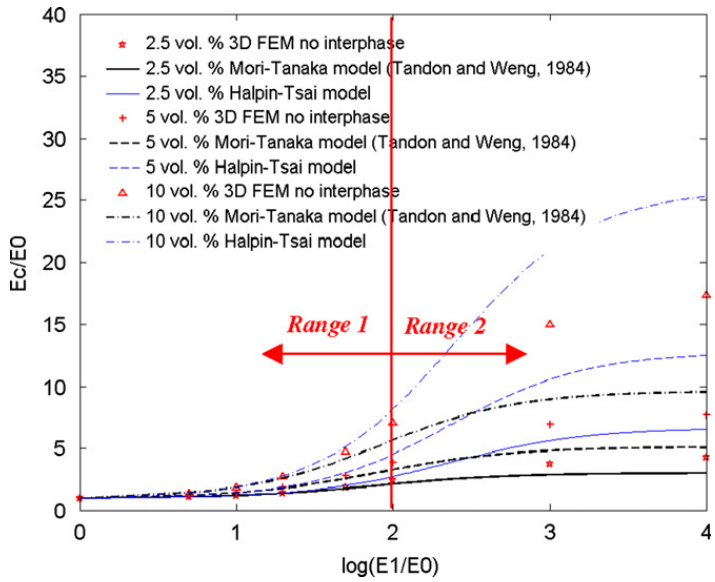


**Fig. 4.** Comparison of the predicted results of the classical two-phase M–T model (by taking $E1/E0=1.001$, and $ti=0.001$ Tp in the HMM, numerically), H–T model, and the 3D FE simulations.

and more sensitive to the morphology of the particles. Then, some basic assumptions of the classical composite theory are violated. The accuracy of the HMM decreases with the increase of the volume fraction and SR (see Fig. 3), which is explained further in the next section.

### 3.2. Non-uniform elastic state in phases

One needs to bear in mind that the controversy in modeling composites reinforced by the ellipsoidal inclusions versus non-ellipsoidal ones (as mentioned in the Introduction) is for two-phase composites. In order to validate the intrinsic consistency of past arguments numerically, we need to first make our model degenerate to a two-phase model. By taking $E1/E0=1$ or $t_i=0$, the three-phase HMM degenerates to the two-phase M–T model. Results of the M–T model shown in Fig. 4 used the closed form expression of Eshelby's tensor for disk-like ellipsoidal inclusions provided by Tandon and Weng (1984), although the inclusions in the FE simulations are prisms. The FE results shown in Fig. 4 are obtained by using the RVEs with no interphase shown in Table 1.

The stress fields[4] of the two extreme cases are shown in Fig. 5: (a) is the stress field of the case with the lowest volume fraction and SR but with the highest M–T accuracy; (b) is the stress field of the case with the highest volume fraction and SR but with the lowest M–T accuracy. It can be seen that in (a), the stress field of the inclusion is uniform over much of its volume, the non-uniformity only occurs within a very small region close to the boundaries of the inclusion; however, in (b), the strain field is highly non-uniform. It is clear that for low values of SR, although the inclusions in the FE simulations are prismatic instead of ellipsoidal, approximate uniform elastic states are generated, and the closed formed Eshelby's tensor and therefore the M–T model have good accuracy. However, the uniformity assumption is violated for cases with high SRs and high volume fractions.

Both Figs. 4 and 5 show that for non-ellipsoidal inclusions, the prediction accuracy of the M–T model is good when the SR is low. With the increase of SR and volume fraction of the inclusion, the accuracies of both the M–T model and the H–T model decrease, which confirms the intrinsic consistency of the arguments in literature on this topic mentioned in the introduction. Actually, the HMM inherits this feature of two-phase M–T model, which is indicated by our numerical results for multi-phase composites shown in Fig. 3.

In addition, Fig. 4 shows that the M–T model under-predicts the 3D FE data; and the H–T model over-predicts both. Sheng et al. (2004) observed a similar phenomenon when comparing the predicted results of the M–T model, the H–T model and 2D plane strain FE simulation data.

The poor accuracy of the M–T model and the HMM at high level of SRs and volume fractions is caused by the non-uniform elastic state in the non-ellipsoidal inclusion, and the increasing sensitivity of the model to the morphology of the nonellipsoidal inclusion with the increase of SR and the volume fraction, which will be explained from an energy point of view in Section 3.3. This observation shows that the morphology of the inclusions is significant to nanocomposites, which usually have a very high stiffness contrast between reinforcement and matrix, although it may not be crucial to composites that do not display such contrast (macro-composites such as traditional fiber reinforced media, where fiber diameters are in the range 5–7 μm and stiffness contrast is 250).

[4] The strain field has the same scenario because of the assumed linear elastic phase behavior, and only the scale is different.

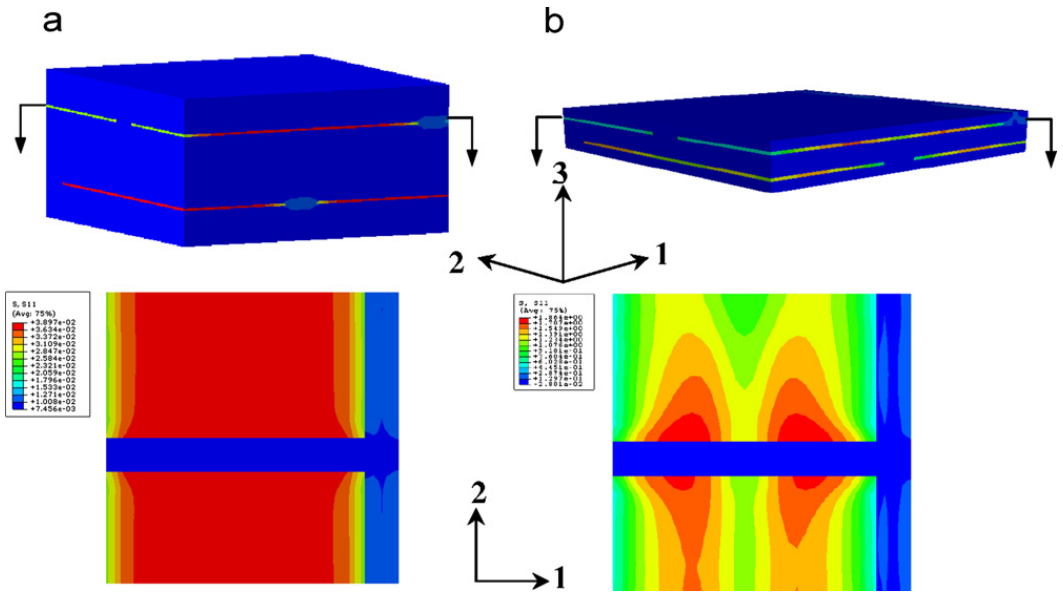


**Fig. 5.** FE results of stress distribution in the inclusion for two representative cases of low and high volume fractions and SRs. (a) Case of 2.5 vol% $E1/E0=5$, with uniform stress field. (b) Case of 10 vol% $E1/E0=10{,}000$, with non-uniform stress field.

### 3.3. *Energy analysis due to the non-uniformity of the stress and strain fields*

In this section, the influence of non-uniformity of the elastic states on the strain energy is explained, which also explains the poor accuracy of the M–T model and the HMM at high level of SR.

Assuming all phases are homogeneous, for the non-uniform stress-strain field, the spatial average stress and strain in each phase can be expressed by Eq. (19) (the sign '$\langle\bullet\rangle$' represents the spatial average)

$$\frac{1}{V^j}\int_{V^j}\underline{\sigma}(\underline{x})dV^j=\left\langle\underline{\sigma}^j\right\rangle=C^j\left\langle\underline{\varepsilon}^j\right\rangle,\ \text{and}\ \frac{1}{V^j}\int_{V^j}\underline{\varepsilon}(\underline{x})dV^j=\left\langle\underline{\varepsilon}^j\right\rangle, \tag{19}$$

where $V^j$ is the volume of phase $j$.

Then the average strain ($\overline{\underline{\varepsilon}}$) and stress ($\overline{\underline{\sigma}}$) are expressed in terms of the phase volume fractions ($f^j$) and their spatial averages by

$$f^j\left\langle\underline{\varepsilon}^j\right\rangle=\overline{\underline{\varepsilon}},\quad f^j\left\langle\underline{\sigma}^j\right\rangle=\overline{\underline{\sigma}},\quad j=1,2,\ldots N, \tag{20}$$

where $N$ is the number of phases in the composite.

These average stress and strain values were checked numerically from the FE results, and were found to be accurate even for the cases with high non-uniformity. The elastic energy $U_{elastic}$ in the RVE is defined as the summation of the elastic energy in all of the phases, which is the *real* elastic energy, as shown below

$$U_{elastic}=\frac{1}{2}\sum_{j=1}^{N}\int_{V^j}\underline{\sigma}(\underline{x})\cdot\underline{\varepsilon}(\underline{x})dV^j=\frac{1}{2}\sum_{j=1}^{N}\int_{V^j}C^j\underline{\varepsilon}(\underline{x})\cdot\underline{\varepsilon}(\underline{x})dV^j=\frac{1}{2}\sum_{j=1}^{N}V^jC^j\left\langle\underline{\varepsilon}(\underline{x})\cdot\underline{\varepsilon}(\underline{x})\right\rangle. \tag{21}$$

The 'uniform energy' $U_{uniform}$ is defined as the total elastic energy when the assumption of uniformity holds, which is the *expected* elastic energy with the assumption of uniformity, as shown below

$$U_{uniform}=\frac{1}{2}\sum_{j=1}^{N}V^jC^j\left\langle\varepsilon^j\right\rangle\cdot\left\langle\varepsilon^j\right\rangle=\frac{V}{2}f^jC^j\left\langle\varepsilon^j\right\rangle\cdot\left\langle\varepsilon^j\right\rangle. \tag{22}$$

Using the Cauchy–Schwarz inequality, we can prove (see Appendix B) that

$$V^j\int_{V^j}\underline{\varepsilon}(\underline{x})\cdot\underline{\varepsilon}(\underline{x})dV^j\geq\int_{V^j}\underline{\varepsilon}(\underline{x})dV^j\cdot\int_{V^j}\underline{\varepsilon}(\underline{x})dV^j, \tag{23}$$

i.e.

$$\left\langle\underline{\varepsilon}(\underline{x})\cdot\underline{\varepsilon}(\underline{x})\right\rangle\geq\left\langle\underline{\varepsilon}(\underline{x})\right\rangle\cdot\left\langle\underline{\varepsilon}(\underline{x})\right\rangle. \tag{24}$$

If and only if $\underline{\varepsilon}(\underline{x})=const.$, i.e. the strain field is uniform, the equalities in Eqs. (23) and (24) hold. Therefore, by combining Eqs. (21)–(24),

$$U_{elastic}\geq U_{uniform}. \tag{25}$$

Similarly, if and only if the strain field is uniform, the equality Eq. (25) holds.

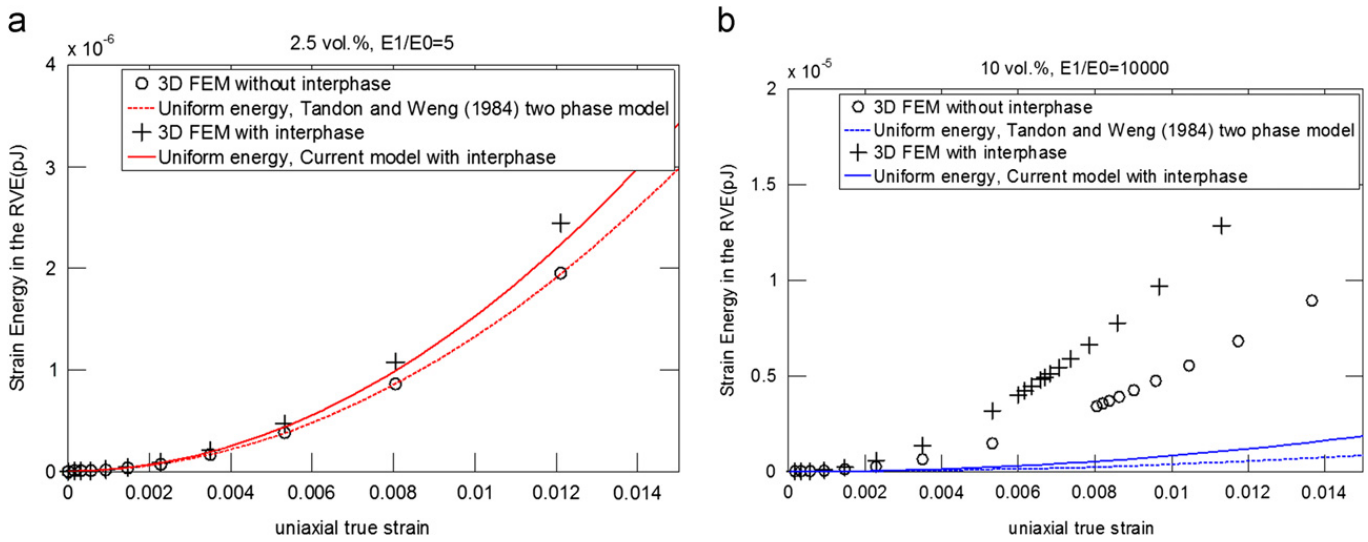


**Fig. 6.** Comparison of $U_{elastic}$ and $U_{uniform}$ with different levels of SR. (a) Uniform and (b) non-uniform.

Eq. (25) shows that the total *real* strain energy of the composite with a non-uniform strain distribution is larger than the total *expected* energy with the assumption of a uniform strain distribution, although the average strain tensor in each phase is the same. In other words, to generate a non-uniform strain field with a certain average value costs more energy than to create a uniform strain field with the same average value of strain, and the difference can be huge for the cases of high non-uniformity. Therefore, the HMM model and M–T model provide the lower bound with the assumption of non-ellipsoidal inclusions and thus the uniform elastic states with high SRs. In fact, the difference between $U_{elastic}$ and $U_{uniform}$ can be an indicator of the level of non-uniformity. In Fig. 6, the results of the energy analysis of the two cases shown in Fig. 5 are shown. The lines represent $U_{uniform}$ (the solid lines represent the cases with interphase, the dash lines represent the cases without interphase); the symbols represents $U_{elastic}$ (the '+' symbols represent the cases with an interphase; the 'o' symbols represent the cases without an interphase). Fig. 6a shows that when the uniformity holds (small volume fraction, small value of SR), $U_{elastic}$ approximately equals $U_{uniform}$; however, when the non-uniformity holds, there is a large difference between $U_{elastic}$ and $U_{uniform}$, shown in Fig. 6b (more than 100 times difference).

## 4. Modification of the HMM

The HMM shows good accuracy in Range 1 of SR, in which the assumption of ellipsoidal inclusions can be relaxed due to the fact that the uniformity holds even for non-ellipsoidal inclusions. In reality, the morphology of the inclusions varies. Specially, for nanocomposites, on one hand, the SRs of nanocomposites fall into Range 2; on the other hand, the inclusions are very likely to be non-ellipsoidal, even irregular. If the volume fraction is low enough, the HMM is still accurate (such as the case with 2.5%, shown in Fig. 3); but for a larger volume fraction, the accuracy of the HMM is not acceptable. This brings limitations to the application of the HMM to nanocomposites directly. Modifications are needed to take the non-uniformity effects into consideration. The modified HMM (MHMM) is developed in this section.

The morphology sensitivity in Range 2, illustrated in Sections 3.2 and 3.3, of non-ellipsoidal inclusions leads to a redistribution of strains between phases compared with those predicted by the HMM with the assumption of ellipsoidal inclusions. Considering the morphology effect, the strategy of the MHMM is to introduce a perturbation strain caused by the morphology effect to each phase. For example, $\delta\underline{\varepsilon}^j$ is introduced to the average strain of the $(j-1)$th phase that is obtained from the HMM, as shown below

$$\underline{C}^j\left(\underline{\varepsilon}^{j-1}+\tilde{\underline{\varepsilon}}^j\right)=\underline{C}^{j-1}\left(\underline{\varepsilon}^{j-1}+\tilde{\underline{\varepsilon}}^j-\underline{\varepsilon}^{j^*}+\delta\underline{\varepsilon}^j\right). \tag{26}$$

$\delta\underline{\varepsilon}^j$ represents the effect of morphology-induced non-uniformity. To keep the stress at the far filed undisturbed, the total additional perturbation stresses causes by $\delta\underline{\varepsilon}^j$ in all phases should be zero. However, the average strain of the composite changes due to this redistribution. Therefore, the general stiffness of the composite is adjusted because of Eq. (13). $\delta\underline{\varepsilon}^j$ is assumed to be proportional to the original strain tensor of the $(j-1)$th phase, thus only scalars $\alpha^j$ are introduced for the modification, while the equivalent transformation strain of the $j$th phase is assumed to be unchanged, shown below

$$\delta\underline{\varepsilon}^j=\alpha^j\underline{\varepsilon}^{j-1},\quad \tilde{\underline{\varepsilon}}^j=\underline{S}_i^j\underline{\varepsilon}^{j^*}, \tag{27}$$

where again the expression for $\underline{S}_i^j$ is provided by Tandon and Weng (1984) as a function of length aspect ratio of the corresponding imaginary two-phase composite is explained in Section 2.2.

Therefore, the hierarchical interaction between the $j$th phase and the $(j-1)$th phase is

$$\underline{\varepsilon}^j = \hat{\underline{T}}_i^j \underline{\varepsilon}^{j-1}, \tag{28}$$

where $\hat{\underline{T}}_i^j$ is the modified dilute concentration tensor that can be derived from Eqs. (26)–(28)

$$\hat{\underline{T}}_i^j = \underline{T}_i^j \left( \underline{I} + \alpha^j \underline{S}_i^j \right). \tag{29}$$

Eq. (29) shows that the stress concentration tensor is modified through the parameters $\alpha^j$. Bradshaw et al. (2003) showed an approach to evaluate the dilute strain concentration tensor, which is used to study the waviness effects of nanotube-reinforced polymer composites. In fact, this approach can be used for evaluating the dilute strain concentration tensor for arbitrary inclusion morphologies numerically through FE simulations with different strain components controlled at the boundaries. However, this approach has limitations when solving inverse problems, in which the nano-structures and the accurate morphologies of the inclusions are not clear, and only macro-mechanical properties can be measured. In these instances (when the morphology is not clear but macroscopic properties are known) , it is practical to do inverse modeling because through the measured macro-stiffness, we can model the morphology effects through the parameters in the MHMM and calibrate them inversely without needing to know the detailed morphology of the nano-particles.

By replacing the dilute stress concentration tensor in Eq. (18), with the modified one in Eq. (29), the stiffness predicted by the MHMM is obtained

$$\hat{\underline{C}}_i = \left[ f^0 \underline{C}^0 + \sum_{j=1}^{K} f^j \left\{ \underline{C}^j \left( \prod_{j=1}^{K} \{ \hat{\underline{T}}_i^j \} \right) \right\} \right] \left[ f^0 \underline{I} + \sum_{j=1}^{k} f^j \left( \prod_{j=1}^{K} \{ \hat{\underline{T}}_i^j \} \right) \right]^{-1}. \tag{30}$$

Using the same concept, the independent multi-phase model can be modified by considering the non-uniformity. The expression of the stiffness tensor is

$$\underline{C}_N = \left[ f^0 \underline{C}^0 + \sum_{j=1}^{N} f^j \{ \underline{C}^j \hat{\underline{T}}^j \} \right] \left[ f^0 \underline{I} + \sum_{j=1}^{N} f^j \{ \hat{\underline{T}}^j \} \right]^{-1}, \tag{31}$$

where

$$\hat{\underline{T}}^j = \underline{T}^j (\underline{I} + \alpha^j \underline{S}^j). \tag{32}$$

Eqs. (26)–(30) are the derivation of the MHMM in the compact form. The morphology parameters $\alpha^j$ are conceptual and provide the simplest expression of this modification in the compact form. For the convenience of the reader to compare the MHMM with the derivation of Tandon and Weng's (1984) model as well as the derivation of the HMM described in Appendix A, the step by step derivation of the MHMM is shown in Appendix C. When implementing the MHMM numerically by following the step by step derivation in Appendix C, a family of parameters $a_j$, which is conceptually equivalent to $\alpha^j$, is used. The reason for choosing $a_j$ is the same as that of choosing $\alpha^j$: make the derivation easier and clearer. For the case with only one interphase layer (then $j=2$), $a_j$ are related to $\alpha^j$ by

$$\alpha^1(\varepsilon_0 + a_2\tilde{\varepsilon}) = (a_1 - a_2)\tilde{\varepsilon}, \quad \alpha^2(\varepsilon_0 + \tilde{\varepsilon} + \varepsilon^{pt1}) = (a_2 - 1)\tilde{\varepsilon}. \tag{33}$$

From Eq. (33), it can be seen that $a_2=1$ corresponds to $\alpha^2=0$, and $\alpha^1=0$ corresponds to $a_1=a_2$. If $a_1=a_2=1$, then $\alpha^1=\alpha^2=0$, and the MHMM degenerates to the HMM.

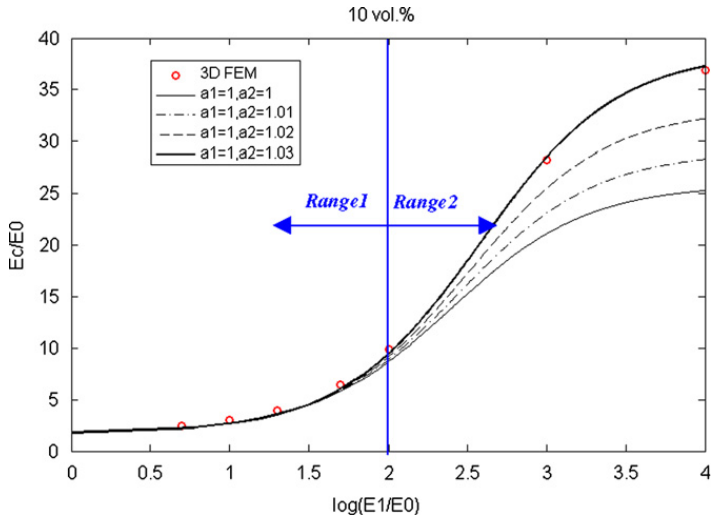


**Fig. 7.** Parameter sensitivity of the MHMM.

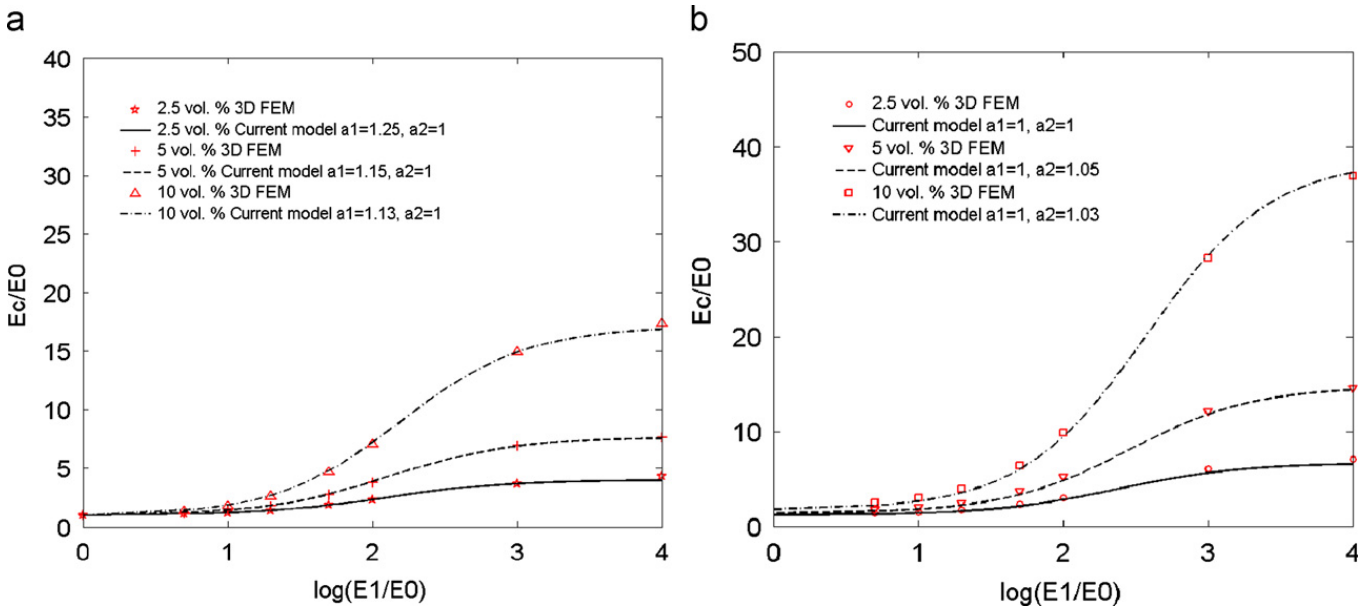


**Fig. 8.** Predicted results of the Modified Hierarchical Multi-interphase Model. (a) No interphase and (b) with interphase.

The predicted results of the MHMM for the case with only one layer of interphase, discussed in Section 3, are shown in Fig. 7. By adjusting only $a_2$, excellent correlation with FE results can be obtained. A comparison of Figs. 3 and 7 shows that with an increase of SR, the MHMM becomes more and more sensitive to $a_2$ (see Fig. 7). When SR is in Range 1, the results of the MHMM are almost the same as those of the HMM. The MHMM can predict the enhancement efficiency accurately over the full range of SR by choosing $a_2$ carefully.

When the MHMM is used for the two-phase composite, changing $a_1$ while keeping $a_2=1$, excellent correlation can again be obtained for the full SR range, see Fig. 8a. For the case with only one interphase layer, changing $a_2$ and keeping $a_1=1$, results in an excellent fit to all of the FE data, as shown in Fig. 8b. It has the trend that the model is more sensitive to the strain perturbation parameters for cases with larger volume fractions or larger SRs.

It is noted that the morphology effect leads to the redistribution of strains between phases. a1 and a2 models this redistribution quantitatively, in this way, a1 and a2 are able to model the influence of the morphology sensitivity.

## 5. Application—shape and size effects

The goal of this section is to show the size-dependency of the HMM by using it to study the effects of particle size and shape on the enhancement efficiency of composites with multi-layered interphase regions. In this section, composites with one interphase layer, which represent the family of composites with multi-layered interphases, are chosen as the study object. All examples used in this section have low volume fractions and small values of SR ($f^p=2.5\%$, SR=100). Therefore, the HMM may be used for these examples without the modifications from Section 4.

### 5.1. Size effects predicted by the HMM

Evidence shows that the thickness and material properties of the interphase region are mainly determined by the chemical and physical characteristics and interactions of the inclusion and the matrix (Smith et al., 2002; Liu et al., 2004; Lyu. et al., 2007). Li et al. (2008a, 2008b) obtained a lower bound for the interphase thickness, about 2 nm for layer-by-layer assembled (LBL) polymer/clay nanocomposites using the Flory–Huggins theory. As before, we retain the assumption that the interphase is a homogenous layer around the inclusion, and its thickness is constant. If the volume fraction of the inclusion is large, the interphase layers around the inclusions may overlap. The ductile to brittle transition of LBL polymer/clay nanocomposites may be predicted by considering this overlapping effect (Li et al., 2008a, 2008b). But this is not the interest of the present study; in this section, we assume that the volume fraction is small enough to avoid the overlapping of interphase layers. Based on these assumptions, Eqs. (34) and (35) are obtained simply from the geometry of the RVE (if the surfaces of the inclusions are convex)

$$f_i \geq \frac{t_i S_p}{V}, \tag{34}$$

$$V = \frac{V_p}{f_p}, \tag{35}$$

where $f_i$ is the volume fraction of the interphase, $t_i$ is the thickness of the interphase, $f_p$ is the volume fraction of the particle, $S_p$ is the surface area of the particle, $V$ is the volume of the RVE and $V_p$ is the volume of the particle. From Eqs. (34) and (35), we get

$$f_i \geq f_p t_i \frac{S_p}{V_p}. \tag{36}$$

Eq. (36) shows that the volume fraction of the interphase, $f_i(f_p,t_i,(S_p/V_p))$, is a function of the volume fraction of the particle, the thickness of the interphase and the surface-to-volume-ratio of the particle. The thinner the interphase, the closer the value of volume fraction of the interphase to this lower bound, predicted by Eq. (36). Since $S_p/V_p$ is size-dependent, $f_i$ is size-independent even if $t_i$ is size-independent. The sketch of this concept is shown in Fig. 9.

Considering the adhesion effects of the polymer chains, shown by many researchers studying polymer composites (Liu and Brinson, 2008; Miwa et al., 2006; Barnard and Curtiss, 2005; Sharma and Ganti, 2004), $t_i$ depends on $S_p/V_p$. Therefore, as a preliminary study, it is further assumed that the interphase thickness is related to $S_p/V_p$ by a power law, shown below

$$t_i = t_0 \left( \frac{S_p V_{p0}}{V_p S_{p0}} \right)^m, \tag{37}$$

where $t_0$ and $S_{p0}/V_{p0}$ are the reference interphase thickness and surface-to-volume-ratio of the inclusion, respectively, for a certain scale of the inclusion. $m(m \geq 0)$ is a material parameter depending on the temperature and the chemical environment of the composite. There are different approaches to determine $t_0$ (Smith et al., 2002; Liu et al., 2004; Lyu. et al., 2007; Li et al., 2008a, 2008b). One of them is through the Flory–Huggins theory (Li et al., 2008a, 2008b; Liu et al., 2004; Lyu et al., 2007), which is within the framework of thermodynamics of polymer blending. When $m=0$, Eq. (37) represents an expression of a size-independent interphase thickness, which applies for all scales of RVEs.

Eqs. (36) and (37) have shown that the volume fraction and the thickness of the interphase change with the size of the inclusion. Then the enhancement efficiency of the composite changes, accordingly. This size effect can be predicted by the HMM quantitatively, which is shown in Fig. 10. The numerical results shown in Fig. 10 are for the cases with the nano-platelet (with the aspect ratio of 1:100) enhanced RVEs, which have been described in Section 3. For all cases shown in Fig. 10, the volume fractions are 2.5%; Young's modulus of the matrix and the platelet are $E0=25$ MPa, $E1=2.5$ GPa,

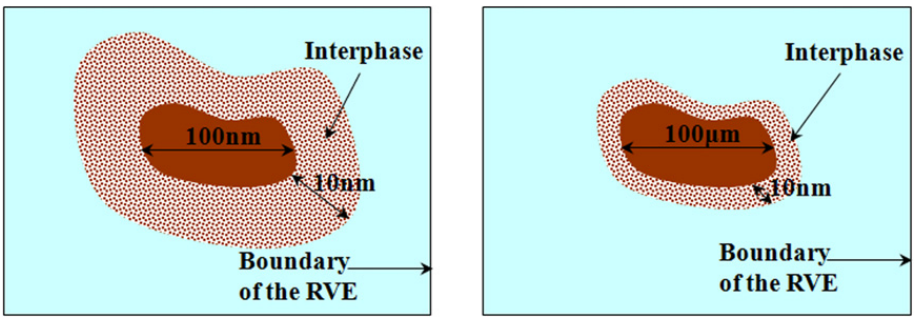


**Fig. 9.** Sketch of the comparison of the composite in different scales (the scale of the interphase is not proportional to those of the RVE and the inclusion but is exaggerated to show this effect clearly).

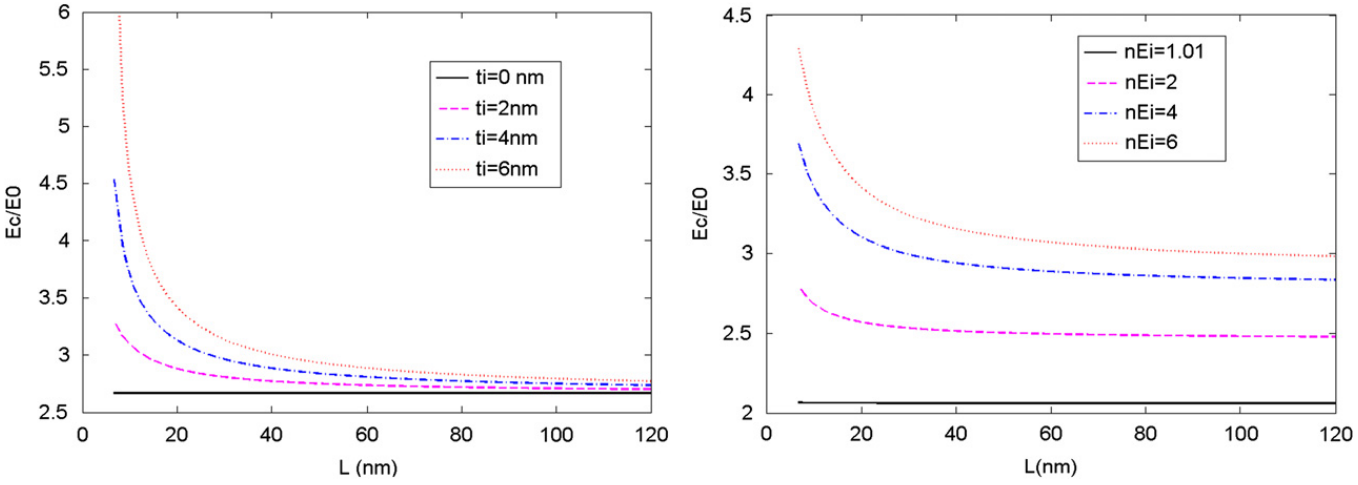


**Fig. 10.** Prediction of particle size effects as well as shape effects with two-step Mori–Tanaka procedure for various constant interphase thickness.

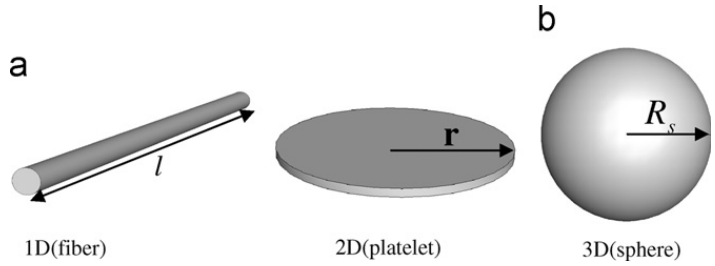


**Fig. 11.** Sketches of typical particle morphology (a) cylindrical; (b) spherical.

respectively; the thickness of the platelet is 1 nm; and $nEi=Ei/E0$, where $Ei$ is the Young's modulus of the interphase. Fig. 10 shows the size-dependency of the HMM, quantitatively: the enhancement efficiency increases dramatically when the characteristic length of the particle decreases; when $t_i=0$, or $nEi=1$, the model degenerates into the classical two-phase Mori–Tanaka model, which is size-independent, as shown by the black solid lines in Fig. 10. It is also shown that with the increasing scale of RVE, the interphase effect diminishes, and eventually the composites become size-independent at relatively larger scales at which the two-phase M–T model reasonably accurate.

### 5.2. Shape-dependency of the surface-to-volume-ratio of the inclusion

The enhancement mechanism described by the HMM is a synergy of several factors, such as the volume fraction of the filler, the thickness of the interphase and the size and the morphology of the filler. The synergistic effects related to the size of the inclusion are mainly due to the fact that some of these factors are related to the size-dependent surface-to-volume-ratio of the inclusion, as illustrated in Section 5.1. Similarly, in order to study the synergistic effects related to the morphology of the inclusion, the shape-dependency of the surface-to-volume ratio needs to be discussed first.

Assuming perfect bonding between phases, the shape-difference of the inclusion can be described by the length aspect ratio and surface-to-volume ratio of the inclusion, quantitatively. Three of the most commonly used shapes of particles for composites are fibers, platelets and spheres. The fiber-like particle and the platelet can be represented by cylinders with different length aspect ratios, as shown in Fig. 11.

Different types of particles with the same volume will have a different surface area. For the spherical particles

$$V=\frac{4}{3}\pi R_s^3,\quad S_s=4\pi R_s^2, \tag{38}$$

where $V$ is the volume of particles, $R_s$ is the radius of the sphere, as denoted in Fig. 11b and $S_s$ is the surface area of the spherical particle. For the cylindrical particle

$$V=\pi r^2 l,\quad S_c=2\pi rl+2\pi r^2, \tag{39}$$

where $r$ and $l$ represent the radius and length of the cylindrical particles, as denoted in Fig. 11. Defining the length aspect ratio as the dominant dimension over the minor dimension of the inclusion, the length aspect ratios of fiber-like particle $n_F$ and that of the platelet $n_p$ are

$$n_F=\frac{l}{2r}, \tag{40}$$

$$n_p=\frac{2r}{l}. \tag{41}$$

The enhancement efficiency of the fiber-like particles and the platelets with the same aspect ratio is compared in this section by taking $n_F=n_P=100$. It should be noted that we are interested in the longitudinal Young's modulus of the reinforcement[5] (along the direction of the dominant dimensions of the particles).

The characteristic length $L$ of particles is defined as

$$L=\sqrt[3]{V}. \tag{43}$$

The surface-to-volume-ratios of spherical, fiber-like and disk-like particles are denoted as $(S/V)_s$, $(S/V)_F$ and $(S/V)_p$, respectively, and are expressed by $L$, as shown below

$$\left(\frac{S}{V}\right)_s=\frac{3}{\sqrt[3]{3/4\pi}L^{-1}}, \tag{44}$$

[5] There are other mechanical properties influenced by the shape of the inclusion besides the longitudinal Young's modulus of the reinforcements. For example, the anisotropy of the composite, the composite with spherical type fillers is 3D isotropic; the composite with aligned platelets is in-plane isotropic; the composite with aligned fibers is 3D anisotropic. We only focus on comparing the longitudinal Young's moduli for the aligned cases that lead to the best enhancement efficiencies that the fillers can achieve.

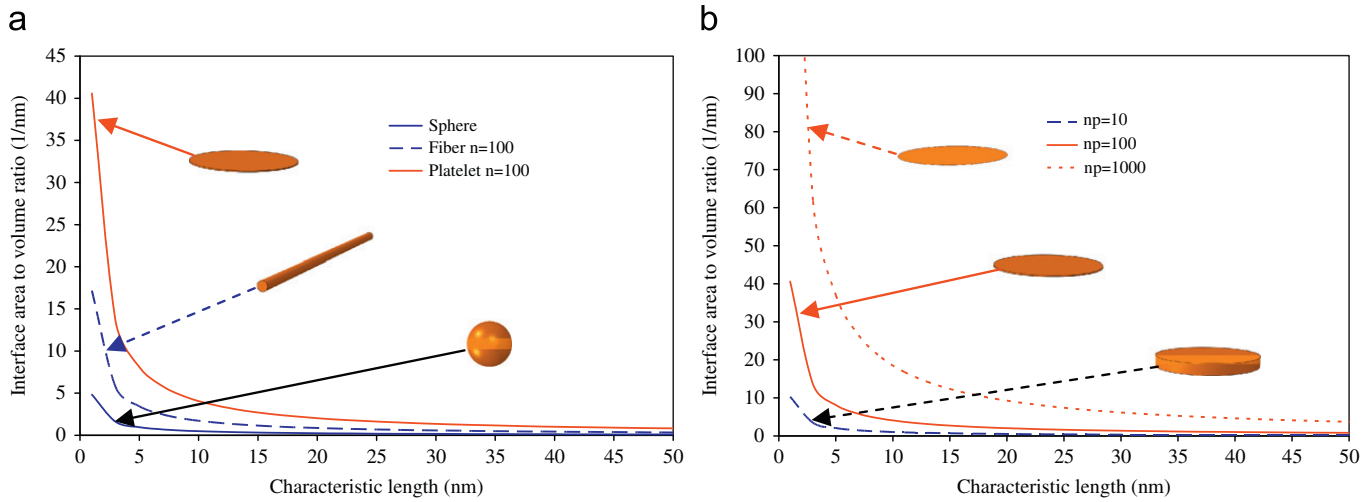


**Fig. 12.** (a) Size effects of the interface area to particle volume fraction for different particle shapes; (b) size effects of the interface area to particle volume fraction for platelet with various aspect ratios.

$$\left(\frac{S}{V}\right)_F = \sqrt[3]{2n_F\pi}\frac{(2n_F+1)}{n_F}L^{-1}, \tag{45}$$

$$\left(\frac{S}{V}\right)_P = \sqrt[3]{2n_P\pi}\frac{(2n_P+1)}{n_P}L^{-1}. \tag{46}$$

Eqs. (44)–(46) are plotted and compared in Fig. 12a, showing that for the same characteristic length, the platelet has a much larger surface-to-volume-ratio than the fiber-like particle and the spherical particle. In other words, the surface-to-volume ratio of the platelet has the strongest size effects in comparison with the other two. Furthermore, for the platelets with different length aspect ratios, as shown in Fig. 12b, the platelet with the larger length aspect ratio shows stronger size effects. As shown in Fig. 12, the surface-to-volume ratios of the particles with different shapes show strong size effects when their characteristic lengths are lower than 20 nm (for example, when the thickness of the platelet with length aspect ratio equaling 100 is 1 nm, the characteristic length of this platelet is 20 nm).

### 5.3. *Shape effects*

The goal of this section is to study the shape-dependent synergistic effects through a parametric analysis of the HMM.

For all the cases studied in this section, taking $f^p$=2.5%, $nEi$=3, $ti$=2 nm, $E0$=25 MPa, $E1$=2.5 GPa, the shapes of the particles as well as the length aspect ratios vary. The parameter describing the relationship between interphase thickness and the surface to volume ratio, denoted by $m$, is also studied.

It is shown in Fig. 13a that with the assumption of the constant interphase thickness ($m$=0), the enhancement efficiencies of all shapes of particles show size effects. The enhancement efficiencies increase with the decrease of the scale. The enhancement efficiency of the sphere is very low (slightly larger than one for most of the scales) due to the low volume fraction and low length aspect ratio, 1. With the same volume fraction and the same length aspect ratio, the fiber has higher enhancement efficiency than the platelet at larger scales[6]; however, when the scale decreases to a certain level, the situation flips, such that the platelet shows higher enhancement efficiency than the fiber, as shown in Fig. 13b. The scale threshold for this flip is larger when $m$ is larger, as can be concluded by comparing Fig. 13a ($m$=0) and Fig. 13b ($m$=1).

With the decrease of the scale, this flip can be explained by the competition between two enhancement mechanisms: one is attributed to the interphase effects, the other purely to the inclusion. Initially (at larger scales), when the interphase effect is weak, the fiber has higher enhancement efficiency than the platelet, which is mainly attributed to the shapes of the inclusions; with the decrease of the scale, since the surface-to-volume-ratio of the platelet increases more rapidly than that of the fiber-like particles, as shown in Fig. 12a, the interphase effects of the platelet increase more rapidly (from Eqs. (36) and (37)). Eventually, when the scale is reduced to the threshold, the interphase effects win and become dominant, and the platelet shows much better enhancement efficiency than the fiber-like particle. This process is predicted by the HMM, as shown in Fig. 13b, in which, when the characteristic length of the inclusion is below 15 nm, the platelet is superior to the fiber with respect to the enhancement efficiency. Thus, platelets are very promising choices of fillers for nanocomposites.

[6] This conclusion is widely recognized in industry: advanced aerospace fiber composite panels are constructed with lamina that have carbon (or glass) fibers whose diameter is about 6–10 μm and this is indeed the correct morphology as predicted by the current study. It is also interesting to note that the fiber morphology is found in birch wood and balsa wood which are used in high stiffness industrial applications. Also, it is observed and studied by Liu and Brinson (2008) that carbon nanotube reinforced samples can achieve a higher level of improvement in properties than using graphite nanoplatelets.

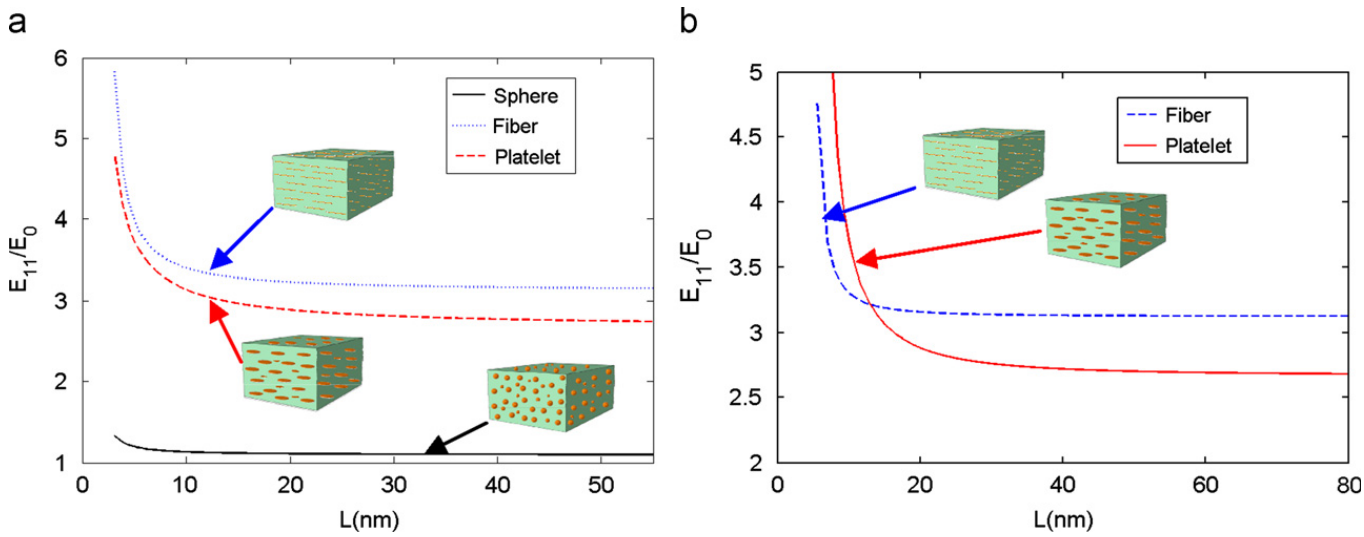


**Fig. 13.** Prediction of size effects of longitudinal Young's modulus of nanocomposite using Hierarchical multi-interphase model with various dependency of interphase thickness on surface to volume ratio of the nano-particles. (a) $m=0$ and (b) $m=1$.

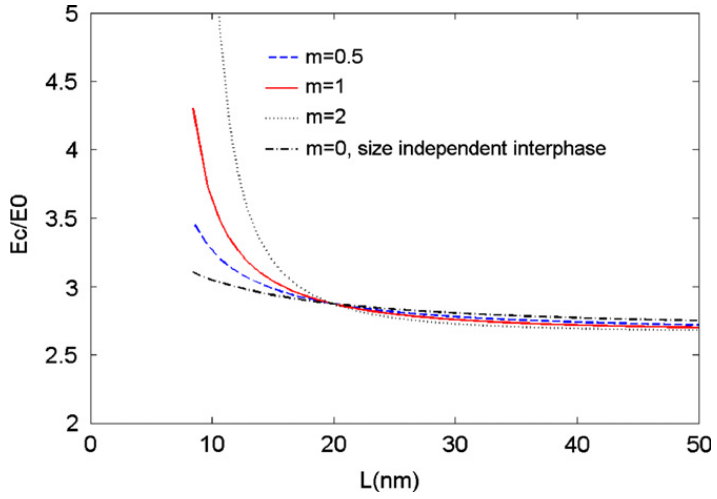


**Fig. 14.** Influence of $m$ on size effects.

In fact, in the current research community, interest has been shown in the platelet-enhanced composites, for example, the studies of the brick–mortar microstructure found in nacre (Podsiadlo et al., 2007; Li et al., 2008, in press; Kaushik et al., 2009).

Therefore, it can be concluded that the morphology of the fillers becomes more and more important when the scale decreases and should be considered in material design.

By only changing $m$ and keeping all other parameters unchanged in the HMM, the influence of $m$ on the enhancement efficiency for the platelet-reinforced nanocomposites is studied and the results are shown in Fig. 14. The intersection of all the curves in Fig. 14 is the reference point in Eq. (37). Fig. 14 shows that, as predicted by the HMM, when the scale is less than that corresponding to the reference point, larger values of $m$, which implies stronger size-dependency of the interphase thickness, lead to better enhancement efficiencies.

## 6. Conclusions and discussion

The influence of interphase layers around nanoinclusions on the elastic properties of nanocomposites has been studied using the analytical Hierarchical Multi-interphase Model developed in the present paper. Different from the two-phase M–T model, the HMM is particle size-dependent. To verify the accuracy of the HMM, the prediction results of the HMM were compared with data obtained from 3D Finite Element simulations. 3D Finite Element models describing the details of the nanostructure of the RVE with the interphase layers were generated and simulations using the commercial package ABAQUS were carried out under displacement controlled conditions along with periodic boundary conditions on the RVE. Simulation results for various volume fractions and stiffness ratios (SRs) have been presented. The HMM is accurate for the cases with low SRs (less than 100).

Since the HMM is based on the M–T model, it inherits the assumptions and therefore some limitations of the M–T model. One of these assumptions is the ellipsoidal morphology of the inclusions and the induced uniformity of stress and strain fields in the inclusions. In this study, it is shown numerically that this assumption of ellipsoidal inclusions can be relaxed for the cases with low volume fractions and low SRs. This observation is also explained from an energy point of view in this paper.

For the cases with high volume fractions and/or high SRs, modification is needed due to the non-uniformity of the stress strain fields in the inclusions. To accommodate this finding, the Modified Hierarchical Multi-interphase Model (MHMM) is proposed here by introducing additional parameters to the HMM. The MHMM is only sensitive to these additional parameters when the volume fractions and/or the SRs are high. For the cases with low volume fractions and/or the SRs, the results of the MHMM are indistinguishable from the HMM. It should be noted that little information for composites in the range of high SR, either experimental or numerical, can be found in the open literature, because traditional composites typically fall out of this range. But for many new nanocomposites, the SRs are very high and no existing analytical models are available for them. The MHMM contributes to close this gap in predictive capability.

Finally, the HMM is used to predict the size effect, shape effects and their interactions quantitatively. The HMM can be used to study how the interphase thickness changes with the surface-to-volume-ratio of the inclusions, a simple power law relation is proposed from the results of a preliminary study. By studying the shape effects predicted through the HMM, it is concluded that although the fiber holds the highest enhancement efficiency for larger scales, with the decrease of the scale, the platelet takes its place gradually. With the decrease of the scale, the inclusion morphology becomes more and more important with respect to the enhancement efficiency and should be considered in material design.

## Appendix A. The HMM

The notation used here is consistent with that in Tandon and Weng (1984). $C^i_{ijkl}$ is the stiffness tensor of the interphase; $\varepsilon^{pt1}_{kl}$ and $\sigma^{pt1}_{kl}$ are the perturbation strain and stress of the interphase from the average stress and strain of the matrix, respectively; $\varepsilon^{pt2}_{kl}$ and $\sigma^{pt2}_{kl}$ are the perturbation strain and stress of the inclusion from the average stress and strain of the interphase, respectively. $\varepsilon^{*1}$ is the equivalent transformation strain between the interphase and matrix, $\varepsilon^{*2}$ is the equivalent transformation strain between the inclusion and the interphase.

After the perturbation, the constitutive relation in the matrix is

$$\overline{\sigma}_{ij}+\tilde{\sigma}_{ij}=C^m_{ijkl}\left(\varepsilon^0_{kl}+\tilde{\varepsilon}_{kl}\right), \tag{A.1}$$

that in the interphase is

$$\overline{\sigma}_{ij}+\tilde{\sigma}_{ij}+\sigma^{pt1}=C^i_{ijkl}\left(\varepsilon^0_{kl}+\tilde{\varepsilon}_{kl}+{\varepsilon_{kl}}^{pt1}\right)=C^m_{ijkl}\left(\varepsilon^0_{kl}+\tilde{\varepsilon}_{kl}+{\varepsilon_{kl}}^{pt1}-{\varepsilon_{kl}}^{*1}\right), \tag{A.2}$$

and that in the inclusion is

$$\overline{\sigma}_{ij}+\tilde{\sigma}_{ij}+\sigma^{pt1}_{ij}+\sigma^{pt2}_{ij}=C^p_{ijkl}\left(\varepsilon^0_{kl}+\tilde{\varepsilon}_{kl}+{\varepsilon_{kl}}^{pt1}+{\varepsilon_{kl}}^{pt2}\right)=C^i_{ijkl}\left(\varepsilon^0_{kl}+\tilde{\varepsilon}_{kl}+{\varepsilon_{kl}}^{pt1}+{\varepsilon_{kl}}^{pt2}-{\varepsilon_{kl}}^{*2}\right). \tag{A.3}$$

The rule of mixtures leads to

$$f_m\tilde{\sigma}_{ij}+f_i(\tilde{\sigma}_{ij}+\sigma^{pt1}_{ij})+f_p(\tilde{\sigma}_{ij}+\sigma^{pt1}_{ij}+\sigma^{pt2}_{ij})=0, \tag{A.4}$$

which means the total perturbation stress is zero.

Assume the stiffness of the interphase is proportional to the stiffness of the matrix

$$C^i_{ijkl}=bC^m_{ijkl}. \tag{A.5}$$

Using Eshelby's solution for two imaginary two-phase composites,

$$\varepsilon^{pt1}_{kl}=S^1_{klmn}\varepsilon^{*1}, \tag{A.6}$$

$$\varepsilon^{pt2}_{kl}=S^2_{klmn}\varepsilon^{*2}. \tag{A.7}$$

Substitute (A.5)–(A.7) into (A.1)–(A.4), we get

$$\varepsilon^0_{kl}=(f_p+f_i-1)S^1_{klmn}\varepsilon^{*1}_{mn}-\left(f_p+f_i+\frac{1}{b-1}\right)\varepsilon^{*1}_{kl}-bf_p\varepsilon^{*2}_{kl}+bf_pS^2_{klmn}\varepsilon^{*2}_{mn}. \tag{A.8}$$

From (A.3) we get

$$\frac{1}{b-1}(bC^m_{ijkl}-C^p_{ijkl})\varepsilon^{*1}_{kl}+(C^p_{ijkl}-bC^m_{ijkl})S^2_{klmn}\varepsilon^{*2}_{mn}+bC^m_{ijkl}\varepsilon^{*2}_{kl}=0. \tag{A.9}$$

(A.8)–(A.9) can be written into matrix form as

$$\begin{bmatrix}\underline{A} & \underline{B}\\ \underline{C} & \underline{D}\end{bmatrix}\begin{bmatrix}\underline{\varepsilon}^{*1}\\ \underline{\varepsilon}^{*2}\end{bmatrix}=\begin{bmatrix}\underline{\varepsilon}^{0}\\ \underline{0}\end{bmatrix}, \tag{A.10}$$

$\underline{\varepsilon}^{*1}$ $\underline{\varepsilon}^{*2}$ can be solved in terms of $\underline{\varepsilon}^0$ as

$$\begin{bmatrix} \underline{\varepsilon}^{*1} \\ \underline{\varepsilon}^{*2} \end{bmatrix} = \begin{bmatrix} \underline{A} & \underline{B} \\ \underline{Cc} & \underline{D} \end{bmatrix}^{-1} \begin{bmatrix} \underline{\varepsilon}^{0} \\ \underline{0} \end{bmatrix}, \tag{A.11}$$

where

$$\begin{aligned} &\underline{A} = (f_i + f_p - 1)\underline{S}^1 - \underline{I}\left[f_i + f_p + \frac{1}{b-1}\right] \\ &\underline{B} = bf_p(\underline{S}^2 - \underline{I}) \\ &\underline{Cc} = \frac{1}{b-1}(b\underline{C}^m - \underline{C}^p) \\ &\underline{D} = (\underline{C}^p - b\underline{C}^m)\underline{S}^2 + b\underline{C}^m. \end{aligned} \tag{A.12}$$

The rule of mixtures for the strains leads to

$$\overline{\varepsilon}_{kl} = f_m(\varepsilon^0_{kl} + \tilde{\varepsilon}_{kl}) + f_i(\varepsilon^0_{kl} + \tilde{\varepsilon}_{kl} + \varepsilon^{pt1}_{kl}) + f_p(\varepsilon^0_{kl} + \tilde{\varepsilon}_{kl} + \varepsilon^{pt1}_{kl} + \varepsilon^{pt2}_{kl}), \tag{A.13}$$

where

$$\tilde{\varepsilon}_{kl} = -(f_i + f_p)(\varepsilon^{pt1}_{kl} - \varepsilon^{*1}_{kl}) - bf_p(\varepsilon^{pt2}_{kl} - \varepsilon^{*2}_{kl}), \tag{A.14}$$

$$\overline{\sigma}_{ij} = C^m_{ijkl}\varepsilon^0_{kl} = C_{ijkl}\overline{\varepsilon}_{kl}.$$

Thus the stiffness matrix of the composite with one layer of interphase $C_{ijkl}$ is solved.

## Appendix B

Let $\psi_1(x)$ and $\psi_2(x)$ be any two real integrable functions in $[a,b]$ then Cauchy–Schwarz inequality is given by

$$\left[\int_a^b \psi_1(x)\psi_2(x)dx\right]^2 \le \int_a^b [\psi_1(x)]^2 dx \int_a^b [\psi_2(x)]^2 dx. \tag{B.1}$$

The equality holds, if and only if

$$\psi_1(x) = \beta\psi_2(x), \tag{B.2}$$

where $\beta$ is a constant.

In this paper, by taking $\psi_2(x)=1$ and $\psi_1(x)=\varepsilon_{ij}(x)$, and extending the one dimensional range $[a,b]$ to the three dimensional space $V^j$, we get

$$V^j \int_{V^j} \underline{\varepsilon}(\underline{x}) \cdot \underline{\varepsilon}(\underline{x}) dV^j \ge \int_{V^j} \underline{\varepsilon}(\underline{x}) dV^j \cdot \int_{V^j} \underline{\varepsilon}(\underline{x}) dV^j,$$

which is Eq. (23) in the text.

## Appendix C. The MHMM

Similar to Appendix A, after the perturbation, the constitutive relation in the matrix is

$$\overline{\sigma}_{ij} + \tilde{\sigma}_{ij} = C^m_{ijkl}(\varepsilon^0_{kl} + a_1\tilde{\varepsilon}_{kl}), \tag{C.1}$$

that in the interphase is

$$\overline{\sigma}_{ij} + \tilde{\sigma}_{ij} + \sigma^{pt1} = C^i_{ijkl}(\varepsilon^0_{kl} + a_2\tilde{\varepsilon}_{kl} + {\varepsilon_{kl}}^{pt1}) = C^m_{ijkl}(\varepsilon^0_{kl} + a_1\tilde{\varepsilon}_{kl} + {\varepsilon_{kl}}^{pt1} - {\varepsilon_{kl}}^{*1}), \tag{C.2}$$

and that in the inclusion is

$$\overline{\sigma}_{ij} + \tilde{\sigma}_{ij} + \sigma^{pt1}_{ij} + \sigma^{pt2}_{ij} = C^p_{ijkl}\left(\varepsilon^0_{kl} + \tilde{\varepsilon}_{kl} + \varepsilon^{pt1}_{kl} + \varepsilon^{pt2}_{kl}\right) = C^i_{ijkl}\left(\varepsilon^0_{kl} + a_2\tilde{\varepsilon}_{kl} + \varepsilon^{pt1}_{kl} + \varepsilon^{pt2}_{kl} - \varepsilon^{*2}_{kl}\right). \tag{C.3}$$

The rule of mixtures leads to

$$f_m\tilde{\sigma}_{ij} + f_i(\tilde{\sigma}_{ij} + \sigma^{pt}_{ij}) + f_p(\tilde{\sigma}_{ij} + \sigma^{pt1}_{ij} + \sigma^{pt2}_{ij}) = 0. \tag{C.4}$$

Noticing (A.5)–(A.7), from (C.1)–(C.4), we get

$$\begin{bmatrix} \underline{Aa} & \underline{Ba} \\ \underline{Ca} & \underline{Da} \end{bmatrix} \begin{bmatrix} \underline{\varepsilon}^{*1} \\ \underline{\varepsilon}^{*2} \end{bmatrix} = \begin{bmatrix} \underline{\varepsilon}^{0} \\ (\underline{C}^p - \underline{C}^m)\underline{\varepsilon}^0 \end{bmatrix}, \tag{C.5}$$

$\underline{\varepsilon}^{*1}$ $\underline{\varepsilon}^{*2}$ can be solved in terms of $\underline{\varepsilon}^0$

$$\begin{bmatrix} \underline{\varepsilon}^{*1} \\ \underline{\varepsilon}^{*2} \end{bmatrix} = \begin{bmatrix} \underline{Aa} & \underline{Ba} \\ \underline{Ca} & \underline{Da} \end{bmatrix}^{-1} \begin{bmatrix} \underline{\varepsilon}^0 \\ (\underline{C}^p - \underline{C}^m)\underline{\varepsilon}^0 \end{bmatrix}, \tag{C.6}$$

where

$$\begin{aligned}
\underline{Aa} &= -\frac{a_2 b - a_1}{a_1(b-1)}\tilde{\underline{A}} - \left[\underline{S}^1 + \frac{1}{b-1}\underline{I}\right] \\
\underline{Ba} &= -\frac{a_2 b - a_1}{a_1(b-1)}\tilde{\underline{B}} \\
\underline{Ca} &= \left(a_1\underline{C}^m - \frac{\underline{C}^p}{a_1}\right)\tilde{\underline{A}} - (\underline{C}^p - \underline{C}^m)\underline{S}^1 - \underline{C}^m \\
\underline{Da} &= \left(a_1\underline{C}^m - \frac{\underline{C}^p}{a_1}\right)\tilde{\underline{B}} - (\underline{C}^p - b\underline{C}^m)\underline{S}^2 - b\underline{C}^m \\
\tilde{\underline{A}} &= -(f_i + f_p)(\underline{S}^1 - \underline{I}) \\
\tilde{\underline{B}} &= -b f_p(\underline{S}^2 - \underline{I}).
\end{aligned} \tag{C.7}$$

The rule of mixtures for the strains leads to

$$\bar{\varepsilon}_{kl} = f_m(\varepsilon^0_{kl} + a_1\tilde{\varepsilon}_{kl}) + f_i(\varepsilon^0_{kl} + a_2\tilde{\varepsilon}_{kl} + \varepsilon^{pt1}_{kl}) + f_p(\varepsilon^0_{kl} + \tilde{\varepsilon}_{kl} + \varepsilon^{pt1}_{kl} + \varepsilon^{pt2}_{kl}). \tag{C.8}$$

Simplify (C.8) as

$$\bar{\underline{\varepsilon}} = \underline{\varepsilon}^0 + \underline{AA}\underline{\varepsilon}^{*1} + \underline{BB}\underline{\varepsilon}^{*2}, \tag{C.9}$$

where

$$\begin{aligned}
\underline{AA} &= \frac{a_1 f_m + a_2 f_i + f_p}{a_1}\tilde{\underline{A}} + (f_i + f_p)\underline{S}^1 \\
\underline{BB} &= \frac{a_1 f_m + a_2 f_i + f_p}{a_1}\tilde{\underline{B}} + f_p\underline{S}^2.
\end{aligned} \tag{C.10}$$

In the end, the strain tensors: perturbation strain in the matrix $\tilde{\varepsilon}$, the strain in the matrix, the interphase and the inclusions $\underline{\varepsilon}^m$, $\underline{\varepsilon}^i$, $\underline{\varepsilon}^p$ can be solved as

$$\begin{aligned}
\tilde{\underline{\varepsilon}} &= \frac{1}{a_1}\begin{bmatrix} \tilde{\underline{A}} & \tilde{\underline{B}} \end{bmatrix} \begin{bmatrix} \underline{\varepsilon}^{*1} \\ \underline{\varepsilon}^{*2} \end{bmatrix} \\
\underline{\varepsilon}^m &= \underline{\varepsilon}^0 + a_1\tilde{\underline{\varepsilon}} \\
\underline{\varepsilon}^i &= \underline{\varepsilon}^0 + a_2\tilde{\underline{\varepsilon}} + \underline{\varepsilon}^{pt1} \\
\underline{\varepsilon}^p &= \underline{\varepsilon}^0 + \tilde{\underline{\varepsilon}} + \underline{\varepsilon}^{pt1} + \underline{\varepsilon}^{pt2}.
\end{aligned} \tag{C.11}$$

## References


Barnard, A.S., Curtiss, L.A., 2005. Computational nano-morphology: modeling shape as well as size. Reviews on Advanced Materials Science 10, 105–109.

Baschnagel, J., Binder, K., 1995. On the influence of hard walls on structural properties in polymer glass simulation. Macromolecules 28, 6808–6818.

Benveniste, Y., 1987. On a new approach to the application of Mori–Tanaka's theory in composite materials. Mechanics of Materials 6 (2), 147–157.

Benveniste, Y., Dvorak, G.J., Chen, T., 1989. Stress fields in composites with coated inclusions. Mechanics of Materials 7, 305–317.

Benveniste, Y., Dvorak, G.J., Chen, T., 1991a. On diagonal and elastic symmetry of the approximate effective stiffness tensor of heterogeneous media. Journal of Mechanics and Physics of Solids 39, 927–946.

Benveniste, Y., Dvorak, G.J., Chen, T., 1991b. On effective properties of composites with coated cylindrically orthotropic fibres. Mechanics of Materials 12, 289–297.

Berryman, J.G., Berge, P.A., 1996. Critique of two explicit schemes for estimating elastic properties of multiphase composites. Mechanics of Materials 22 (2), 149–164.

Bradshaw, R.D., Fisher, F.T., Brison, L.C., 2003. Fiber waviness in nanotube-reinforced polymer composites—II: modeling via numerical approximation of the dilute strain concentration tensor. Composites Science and Technology 63, 1705–1722.

Budiansky, B., 1965. On the elastic moduli of some heterogeneous materials. Journal of Mechanics and Physics of Solids 13, 223–227.

Castaneda, P., Willis, J.R., 1995. The effect of spatial distribution on the effective behavior of composite materials and cracked media. Journal of the Mechanics and Physics of Solids 43, 1919–1951.

Chen, T., Dvorak, G.J., Benveniste, Y., 1990. Stress fields in composites reinforced with cylindrically orthotropic fibres. Mechanics of Materials 9, 17–32.

Christensen, R.M., Lo, K.H., 1979. Solution for effective shear properties in three phase sphere and cylinder models. Journal of Mechanics and Physics of Solids 27 (4), 315–330.

Dai, L.H., Huang, Z.P., Wang, R., 1998. A Generalize self-consistent Mori—Tanaka Scheme for prediction of the effective elastic moduli of hybrid multiphase particulate composites. Polymer Composite 19 (5), 506–513.

Eshelby, J.D., 1957. The determination of the elastic field of an ellipsoidal inclusion and related problems. Proceedings of the Royal Society London, Series A A241, 376–396.

Eshelby, J.D., 1959. The elastic field outside an ellipsoidal inclusion. Proceedings of the Royal Society London, Series A A252, 561–569.

Eshelby, J.D., 1961. Elastic inclusions and inhomogeneities. In: Sneddon, I.N., Hill, R. (Eds.), Progress in Solid Mechanics, 2. North Holland, Amsterdam, pp. 89–140.
Fertig III, R.S., Garnich, M.R., 2004. Influence of constituent properties and microstructural parameters on the tensile modulus of a polymer/clay nanocomposite. Composites Science and Technology 64, 2577–2588.
Fossey,S., 2002. Atomistic modeling of polymer matrices in nanocomposites. Nanocomposites 2002: delivering new value to polymers conference proceedings. Executive Conference Management, San Diego, CA.
Ginzburg, V.V., Balazs, A.C., 1999. Calculating phase diagrams of polymer-platelet mixtures using density functional theory: implications for polymer/clay composites. Macromolecules 32, 5681–5688.
Hbaieb, K., Wang, Q.X., Chia, Y.H.J., Cotterell, B., 2007. Modelling stiffness of polymer/clay nanocomposite. Polymer 48, 901–909.
Helfand, E., Tagami, Y., 1972. Theory of the interface between immiscible polymers. II. Journal of Chemistry and Physics 56, 3592–3601.
Hill, R., 1965. A self-consistent mechanics of composite materials. Journal of Mechanics and Physics of Solids 13, 213–222.
Huang, Y., Hu, K.X., Wei, X., Chandra, A., 1994. A Generalized self-consistent mechanics method for composite materials with multiphase inclusions. Journal of Mechanics and Physics of Solids 42, 491.
Ji, X.L., et al., 2002. Tensile modulus of polymer nanocomposites. Polymer Engineering and Science 42 (5), 983–993.
Jiang, L.Y., Huang, Y., Jiang, H., Ravichandran, G., Gao, H., Hwang, K.C., Liu, B., 2006. A cohesive law for carbon nanotube/polymer interfaces based on the van der Waals force. Journal of the Mechanics and Physics of Solids 54, 2436–2452.
Kaushik, A.K., Podsiadlo, P., Qin, M., Shaw, C.M., Waas, A.M., Kotov, N.A., Arruda, E.M., 2009. The role of nanoparticle separation in the finite deformation response of polyurethane–clay nanocomposites. Macromolecules 42 (17), 6588–6955.
Li, J.Y., 1999. On micromechanics approximation for the effective thermoelastic moduli of multiphase composite materials. Mechanics of Materials 31, 149–159.
Li, Y., Waas, A.M., Arruda, E.M., 2008a. A particle size-shape-dependent three-phase two-step Mori–Tanaka method for studying of the interphase and particle size and shape effects of polymer/clay nanocomposites. In: Proceeding of the 2008 ASME International Mechanical Engineering Congress & Exposition (IMECE), vol. 13, pp. 225–232.
Li, Y., Waas, A.M., Arruda, E.M., 2008b. A non-local visco-plastic model with strain gradient effects and interphase effects for simulating the stiffness and yield strength of a class of polymer nanocomposites. In: Proceeding of the 2008 ASME International Mechanical Engineering Congress & Exposition (IMECE), vol. 13, pp. 1119–1126.
Li, Y., Waas, A.M., Arruda, E.M., 2010. The effects of the interphase and strain gradients on the elasticity of layer by layer (LBL) polymer/clay nanocomposites. International Journal of Solids and Structures, in review.
Lim, T.C., 2003. Simplified model for the influence of inclusion aspect ratio on the stiffness of aligned reinforced composites. Journal of Reinforced Plastics and Composites 22 (4), 301–325.
Lim, T.C., 2005. Size-dependency of nano-scale inclusions. Journal of Materials Science 40, 3841–3842.
Lipatov, Y.S., Nesterov, A.E., 1997. Thermodynamics of polymer blends. Polymer Thermodynamics Library vol1.
Liu, H., Brinson, L.C., 2006. A hybrid numerical–analytical method for modeling the viscoelastic properties of polymer nanocomposites. Transactions of the ASME Vol. 73, 758–768.
Liu, H., Brinson, L.C., 2008. Reinforcing efficiency of nanoparticles: a simple comparison for polymer nanocomposites. Composite Science and Technology 68, 1502–1512.
Liu, R.Y.F., Bernal-Lara, T.E., et al., 2004. Interphase materials by forced assembly of glassy polymers. Macromolecules 37, 6972–6979.
Liu, X., Hu, G., 2005. Contimuum micromechanical theory of overall plasticity for particulate composites including particle size effect. International Journal of Plasticity 21, 777–799.
Lyu, S., Grailera, T., Belua, A., Schleya, J., Bartletta, T., Hobota, C., Sparera, R., Unterekera, D., 2007. Nano-adsorbents control surface properties of polyurethane. Polymer 48 (20), 6049–6055.
Markenscoff, X., 1998. On the shape of the Eshelby inclusions. Journal of Elasticity 49, 163–166.
Mori, T., Tanaka, K., 1973. Average stress in matrix and average elastic energy of materials with misfitting inclusions. Acta Metallurgica et Materialia 21, 571–574.
Miwa, Y., Drews, A.R., Schlick, S., 2006. Detection of the direct effect of clay on polymer dynamics: the case of spin-labeled poly (methyl acrylate)/clay nanocomposites studied by ESR, XRD, and DSC. Macromolecules 39, 3304–3311.
Mura, T., Shodja, H.M., Lin, T.Y., Safadi, A., Makkawy, A., 1994. The determination of the elastic field of a pentagonal star shaped inclusion. Bulletin of the Technical University of Istanbul 47, 267–280.
Nozaki, H., Taya, M., 1997. Elastic fields in a polygon-shaped inclusion with uniform eigenstrains. Journal of Applied Mechanics 64, 495–502.
Nozaki, H., Taya, M., 2001. Elastic fields in a polyhedral inclusion with uniform eigenstrains and related problems. Journal of Applied Mechanics 68, 441–452.
Podsiadlo, P., Kaushik, A.K., Arruda, E.M., Waas, A.M., Shim, B.S., Xu, J., Nandivada, H., Pumplin, B.G., Lahann, J., Ramamoorthy, A., Kotov, N.A., 2007. Ultrastrong and stiff layered polymer nanocomposites. Science 318, 80–83.
Podsiadlo, P., Kaushik, A.K., Shim, B.B., Agarwal, A., Tang, Z., Waas, A.M., Arruda, E.M., Kotov, N.A., 2008. Can nature's design be improved upon high strength nacre-like nanocomposites. Journal of Physical Chemistry C.
Rodin, G.J., 1996. Eshelby's inclusion problem for polygons and polyhedral. Journal of the Mechanics and Physics of Solids 44 (12), 1977–1995.
Rodin, G.J., 1998. Discussion of "Elastic fields in a polygon-shaped inclusion with uniform eigenstrains," by N. Nozaki and M. Taya. Journal of Applied Mechanics 6 (5), 278.
Sarvestani, A.S., 2003. On the overall elastic moduli of composites with spherical coated fillers. International Journal of Solids and Structures 40 (26), 7553–7566.
Schjodt-Thomsen, J., Pyrz, R., 2001. The Mori–Tanaka stiffness tensor: diagonal symmetry, complex fibre orientations and non-dilute volume fractions. Mechanics of Materials 33, 531–544.
Sharma, P., Ganti, S., 2004. Size-dependent Eshelby's tensor for embedded nano-inclusions incorporating surface/interface energies. Journal of Applied Mechanics 71, 663–671.
Sheng, N., Boyce, M.C., Parks, D.M., Rutledge, G.C., Abes, J.I., Cohen, R.E., 2004. Multiscale micromechanical modeling of polymer/clay nanocomposites and the effective clay particle. Polymer 45, 487–506.
Shodja, H.M., Sarvestani, A.S., 2001. Elastic fields in double inhomogeneity by the equivalent inclusion method. ASME Journal of Applied Mechanics 68 (1), 3–10.
Smith, G.D., et al., 2002. A molecular dynamics simulation study of the viscoelastic properties of polymer nanocomposites. Journal of Chemistry and Physics 117 (20), 9478–9489.
Tan, H., Huang, Y., Liu, C., Geubelle, P.H., 2005. The Mori–Tanaka method for composite materials with nonlinear interface debonding. International Journal of Plasticity 21, 1890–1918.
Tandon, G.P., Weng, G.J., 1984. The effect of aspect ratio of inclusions on the elastic properties of unidirectionally aligned composites. Polymer Composites 5 (4), 327–333.
Tandon, G.P., Weng, G.J., 1986. Average stress in the matrix and effective moduli of randomly orientated composites. Composite Science and Technology 27, 111–132.
Taya, M., Chou, T.-W., 1981. On two kinds of ellipsoidal inhomogeneities in an infinite elastic body: an application to a hybrid composite. International Journal of Solids and Structures 17, 553–563.
Taya, M., Mura, T., 1981. International Journal of Applied Mechanics 48, 361.

Vernerey, F.J., Liu, W.K., Moran, B., Olson, G., 2008. A micromorphic model for the multiple scale failure of heterogeneous materials. Journal of the Mechanics and Physics of Solids 56, 1320–1347.
Wu, Y., Ling, Z., Dong, Z., 1999. Stress–strain fields and the effectiveness shear properties for three-phase composites with imperfect interface. International Journal of Solids and Structures 37, 1275–1292.
Yung, K.C., Wang, J., Yue, T.M., 2006. Modeling Young's modulus of polymer-layered silicate nanocomposites using a modified Halpin–Tsai micromechanical model. Journal of Reinforced Plastics and Composites 25, 847–860.